SIAM J. IMAGING SCIENCES
Vol. 12, No. 2, pp. 809–838

Inverse Obstacle Scattering for Elastic Waves with Phased or Phaseless Far-Field Data*

Heping Dong†, Jun Lai‡, and Peijun Li§

Abstract. This paper concerns an inverse elastic scattering problem which is to determine the location and the shape of a rigid obstacle from the phased or phaseless far-field data for a single incident plane wave. By introducing the Helmholtz decomposition, the model problem is reduced to a coupled boundary value problem of the Helmholtz equations. The relation is established between the compressional or shear far-field pattern for the elastic wave equation and the corresponding far-field pattern for the coupled Helmholtz equations. An efficient and accurate Nyström-type discretization for the boundary integral equation is developed to solve the coupled system. The translation invariance of the phaseless compressional and shear far-field patterns are proved. A system of nonlinear integral equations is proposed and two iterative reconstruction methods are developed for the inverse problem. In particular, for the phaseless data, a reference ball technique is introduced to the scattering system in order to break the translation invariance. Numerical experiments are presented to demonstrate the effectiveness and robustness of the proposed method.

Key words. elastic wave equation, inverse obstacle scattering, phaseless data, boundary integral equations, Helmholtz decomposition

AMS subject classifications. 78A46, 65N21

DOI. 10.1137/18M1227263

1. Introduction.

Scattering problems for elastic waves have significant applications in seismology and geophysics [30]. As an important research topic in scattering theory, the inverse obstacle scattering problem (IOSP) is to identify unknown objects that are not accessible by direct observation through the use of waves. The IOSP for elastic waves has continuously attracted much attention by many researchers. The recent development can be found in [2] on mathematical and numerical methods for solving the IOSP in elasticity imaging.

The phased IOSP refers to the IOSP using full scattering data which contains both phase and amplitude information. The phased IOSP for elastic waves has been extensively studied and a great deal of mathematical and numerical results are available. In [31, 32, 36], the

*Received by the editors November 16, 2018; accepted for publication (in revised form) March 13, 2019; published electronically May 9, 2019.

http://www.siam.org/journals/siims/12-2/M122726.html

Funding: The work of the first author was partially supported by the National Natural Science Foundation of China grants 11801213 and 11771180. The work of the second author was partially supported by the Funds for Creative Research Groups of the National Natural Science Foundation of China grant 11621101, the Major Research Plan of the National Natural Science Foundation of China grant 91630309, the National Natural Science Foundation of China grant 11871427, and the Fundamental Research Funds for the Central Universities.

†School of Mathematics, Jilin University, Changchun, Jilin 130012, People's Republic of China (dhp@jlu.edu.cn).

‡School of Mathematical Sciences, Zhejiang University, Hangzhou, Zhejiang 310027, People's Republic of China (laijun6@zju.edu.cn).

§Corresponding author. Department of Mathematics, Purdue University, West Lafayette, IN 47907 (lipeijun@math.purdue.edu).

domain derivatives were investigated by using either the boundary integral equation method or the variational method. In [42], based on the Helmholtz decomposition, the boundary value problem of the Navier equation was converted into a coupled boundary value problem of the Helmholtz equations. A frequency continuation method was developed to reconstruct the shape of the obstacles. We refer to [14, 11] for the uniqueness results on the inverse elastic obstacle scattering problem. Related work can be found in [29, 7, 15, 20, 25, 40, 16, 37] on the general inverse scattering problems for elastic waves.

In many practical applications, the phase of a signal either can be very difficult to measure or cannot be measured accurately compared with its amplitude or intensity. Thus it is often desirable to solve the problems with phaseless data, which are called phase retrieval problems in optics or the physical and engineering sciences. Due to the translation invariance property of the phaseless wave field, it is impossible to reconstruct uniquely the location of the unknown objects, which makes the phaseless inverse scattering problems much more difficult compared to the phased case. Various numerical methods have been proposed to solve the phaseless IOSP for acoustic waves governed by the scalar Helmholtz equation. In [28], Kress and Rundell proposed a Newton's iterative method for imaging a two-dimensional sound-soft obstacle from the phaseless far-field data with one incident wave. A nonlinear integral equation method was developed in [17, 18] for the two- and three-dimensional shape reconstruction from a given incident field and the modulus of the far-field data, respectively. The nonlinear integral equation method proposed by Johansson and Sleeman [19] was extended to reconstruct the shape of a sound-soft crack by using phaseless far-field data for one incident plane wave in [12]. In addition, a fundamental solution method [21] and a hybrid method [33] were proposed to detect the shape of a sound-soft obstacle by use of the modulus of the far-field data for one incident field. To overcome the nonuniqueness issue, Zhang and Zhang [45, 46] proposed to use superposition of two plane waves with different incident directions as the illuminating field to recover both of the location and the shape of an obstacle simultaneously by using phaseless far-field data. Recently, a reference ball technique was developed in [10] to break the translation invariance and reconstruct both the location and shape of an obstacle from phaseless far-field data for one incident plane wave. We refer to [41, 38, 43] for the uniqueness results on the inverse scattering problems by using phaseless data. Related phaseless inverse scattering problems as well as numerical methods may be found in [3, 34, 8, 6, 5, 39, 44, 22, 23].

In this paper, we consider the inverse elastic scattering problem of determining the location and shape of a rigid obstacle from phased or phaseless far-field data for a single incident plane wave. Motivated by the recent work in [10, 12], the reference ball technique in [35, 43], and the Helmholtz decomposition in [42], we propose a nonlinear integral equation method combined with the reference ball technique to solve the IOSP for elastic waves. In particular, for the phaseless IOSP, since the location of the reference ball is known, the method has the capability of calibrating the scattering system so that the translation invariance does not hold anymore. Therefore, the location information of the obstacle can be recovered with negligible additional computational costs. Moreover, we develop a Nyström-type discretization for the integral equation to efficiently and accurately solve the direct obstacle scattering problem for elastic waves. It is worth mentioning that the proposed methods for phased and phaseless IOSP are extremely efficient since we only need to solve the scalar Helmholtz equations and avoid solving the vector Navier equations. The goal of this work is fivefold: establish

the relationship between the compressional or shear far-field pattern for the Navier equation and the corresponding far-field pattern for the coupled Helmholtz system; prove the translation invariance property of the phaseless compressional and shear far-field pattern; develop a Nyström discretization for the boundary integral equation to solve the direct obstacle scattering problems for elastic waves; propose a nonlinear integral equation method to reconstruct the obstacle's location and shape by using far-field data for one incident plane wave; develop a reference ball based nonlinear integral equation method to reconstruct the obstacle's location and shape by using phaseless far-field data for one incident plane wave.

The paper is organized as follows. In section 2, we introduce the problem formulation. Section 3 establishes the relationship of the far-field patterns between the elastic wave equation and the coupled Helmholtz system. In section 4, a Nyström-type discretization is developed to solve the coupled boundary value problem of the Helmholtz equations. In section 5, a nonlinear integral equation method and a reference-ball-based iterative method are presented to solve the phased and phaseless IOSP, respectively. Numerical experiments are shown to demonstrate the feasibility of the proposed methods in section 6. The paper is concluded with some general remarks and directions for future work in section 7.

2. Problem formulation. Consider a two-dimensional elastically rigid obstacle, which is described as a bounded domain $D \subset \mathbb{R}^2$ with $\mathcal{C}^2$ boundary Γ_D. Denote by $\nu = (\nu_1, \nu_2)^\top$ and $\tau = (\tau_1, \tau_2)^\top$ the unit normal and tangential vectors on Γ_D, respectively, where $\tau_1 = -\nu_2, \tau_2 = \nu_1$. The exterior domain $\mathbb{R}^2 \setminus \overline{D}$ is assumed to be filled with a homogeneous and isotropic elastic medium with a unit mass density.

Let the obstacle be illuminated by a time-harmonic plane wave $\boldsymbol{u}^{\text{inc}}$, which satisfies the two-dimensional Navier equation

$$\mu \Delta \boldsymbol{u}^{\text{inc}} + (\lambda + \mu) \nabla \nabla \cdot \boldsymbol{u}^{\text{inc}} + \omega^2 \boldsymbol{u}^{\text{inc}} = 0 \quad \text{in } \mathbb{R}^2 \setminus \overline{D},$$

where $\omega > 0$ is the angular frequency and λ, μ are the Lamé constants satisfying $\mu > 0, \lambda + \mu > 0$. Explicitly, we have

$$\boldsymbol{u}^{\text{inc}}(x) = d \mathrm{e}^{\mathrm{i}\kappa_{\text{p}} d \cdot x} \quad \text{or} \quad \boldsymbol{u}^{\text{inc}}(x) = d^{\perp} \mathrm{e}^{\mathrm{i}\kappa_{\text{s}} d \cdot x},$$

where the former is the compressional plane wave and the latter is the shear plane wave. Here $d = (\cos\theta, \sin\theta)^\top$ is the unit propagation direction vector, $\theta \in [0, 2\pi)$ is the incident angle, $d^{\perp} = (-\sin\theta, \cos\theta)^\top$ is an orthonormal vector of d, and

$$\kappa_{\text{p}} = \frac{\omega}{\sqrt{\lambda + 2\mu}}, \quad \kappa_{\text{s}} = \frac{\omega}{\sqrt{\mu}}$$

are the compressional wavenumber and the shear wavenumber, respectively.

The displacement of the total field $\boldsymbol{u}$ also satisfies the Navier equation

$$\mu \Delta \boldsymbol{u} + (\lambda + \mu) \nabla \nabla \cdot \boldsymbol{u} + \omega^2 \boldsymbol{u} = 0 \quad \text{in } \mathbb{R}^2 \setminus \overline{D}.$$

Since the obstacle is rigid, the total field $\boldsymbol{u}$ satisfies

$$\boldsymbol{u} = 0 \quad \text{on } \Gamma_D.$$

The total field $\boldsymbol{u}$ consists of the incident field $\boldsymbol{u}^{\text{inc}}$ and the scattered field $\boldsymbol{v}$, i.e.,

$$\boldsymbol{u} = \boldsymbol{u}^{\text{inc}} + \boldsymbol{v}.$$

It is easy to verify that the scattered field $\boldsymbol{v}$ satisfies the boundary value problem

$$\begin{cases} \mu\Delta\boldsymbol{v} + (\lambda+\mu)\nabla\nabla\cdot\boldsymbol{v} + \omega^2\boldsymbol{v} = 0 & \text{in } \mathbb{R}^2\setminus\overline{D}, \\ \boldsymbol{v} = -\boldsymbol{u}^{\text{inc}} & \text{on } \Gamma_D. \end{cases} \tag{2.1}$$

In addition, the scattered field $\boldsymbol{v}$ is required to satisfy the Kupradze–Sommerfeld radiation condition

$$\lim_{\rho\to\infty}\rho^{\frac{1}{2}}(\partial_\rho\boldsymbol{v}_{\text{p}} - \mathrm{i}\kappa_{\text{p}}\boldsymbol{v}_{\text{p}}) = 0, \quad \lim_{\rho\to\infty}\rho^{\frac{1}{2}}(\partial_\rho\boldsymbol{v}_{\text{s}} - \mathrm{i}\kappa_{\text{s}}\boldsymbol{v}_{\text{s}}) = 0, \quad \rho = |x|,$$

where

$$\boldsymbol{v}_{\text{p}} = -\frac{1}{\kappa_{\text{p}}^2}\nabla\nabla\cdot\boldsymbol{v}, \quad \boldsymbol{v}_{\text{s}} = \frac{1}{\kappa_{\text{s}}^2}\mathbf{curl}\,\mathrm{curl}\boldsymbol{v},$$

are known as the compressional and shear wave components of $\boldsymbol{v}$, respectively. Given a vector function $\boldsymbol{v} = (v_1, v_2)^\top$ and a scalar function v, define the scalar and vector curl operators:

$$\mathrm{curl}\boldsymbol{v} = \partial_{x_1}v_2 - \partial_{x_2}v_1, \quad \mathbf{curl}\,v = (\partial_{x_2}v, -\partial_{x_1}v)^\top.$$

For any solution $\boldsymbol{v}$ of the elastic wave equation (2.1), the Helmholtz decomposition reads

$$\boldsymbol{v} = \nabla\phi + \mathbf{curl}\,\psi, \tag{2.2}$$

where ϕ, ψ are scalar potential functions. Combining (2.2) and (2.1), we may obtain the Helmholtz equations

$$\Delta\phi + \kappa_{\text{p}}^2\phi = 0, \quad \Delta\psi + \kappa_{\text{s}}^2\psi = 0.$$

As usual, the potentials ϕ, ψ are required to satisfy the Sommerfeld radiation conditions

$$\lim_{\rho\to\infty}\rho^{\frac{1}{2}}(\partial_\rho\phi - \mathrm{i}\kappa_{\text{p}}\phi) = 0, \quad \lim_{\rho\to\infty}\rho^{\frac{1}{2}}(\partial_\rho\psi - \mathrm{i}\kappa_{\text{s}}\psi) = 0, \quad \rho = |x|.$$

Combining the Helmholtz decomposition and boundary condition on Γ_D yields that

$$\boldsymbol{v} = \nabla\phi + \mathbf{curl}\,\psi = -\boldsymbol{u}^{\text{inc}}.$$

Taking the dot product of the above equation with ν and τ, respectively, we get

$$\partial_\nu\phi + \partial_\tau\psi = f_1, \quad \partial_\tau\phi - \partial_\nu\psi = f_2,$$

where

$$f_1 = -\nu\cdot\boldsymbol{u}^{\text{inc}}, \quad f_2 = -\tau\cdot\boldsymbol{u}^{\text{inc}}.$$

In summary, the scalar potential functions ϕ, ψ satisfy the coupled boundary value problem

$$\begin{cases} \Delta\phi + \kappa_{\text{p}}^2\phi = 0, \quad \Delta\psi + \kappa_{\text{s}}^2\psi = 0 & \text{in } \mathbb{R}^2\setminus\overline{D}, \\ \partial_\nu\phi + \partial_\tau\psi = f_1, \quad \partial_\tau\phi - \partial_\nu\psi = f_2 & \text{on } \Gamma_D, \\ \lim\limits_{\rho\to\infty}\rho^{\frac{1}{2}}(\partial_\rho\phi - \mathrm{i}\kappa_{\text{p}}\phi) = 0, \quad \lim\limits_{\rho\to\infty}\rho^{\frac{1}{2}}(\partial_\rho\psi - \mathrm{i}\kappa_{\text{s}}\psi) = 0, & \rho = |x|. \end{cases} \tag{2.3}$$

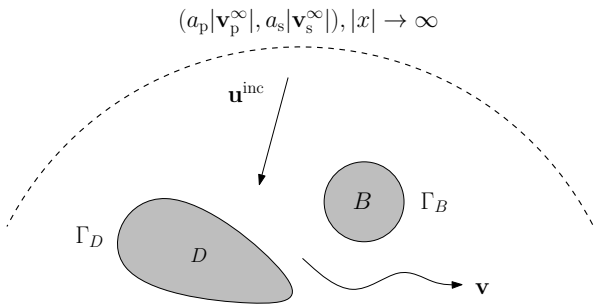

Figure 1. *The problem geometry of elastic obstacle scattering.*

It is well known that a radiating solution of (2.1) has the asymptotic behavior of the form

$$\boldsymbol{v}(x) = \frac{e^{i\kappa_p|x|}}{\sqrt{|x|}}\boldsymbol{v}_p^\infty(\hat{x}) + \frac{e^{i\kappa_s|x|}}{\sqrt{|x|}}\boldsymbol{v}_s^\infty(\hat{x}) + \mathcal{O}\left(\frac{1}{|x|^{\frac{3}{2}}}\right), \quad |x| \to \infty$$

uniformly in all directions $\hat{x} := x/|x|$, where $\boldsymbol{v}_p^\infty$ and $\boldsymbol{v}_s^\infty$, defined on the unit circle Ω, are known as the compressional and shear far-field pattern of $\boldsymbol{v}$, respectively. Define $(a_p, a_s) := (1, 0)$ or $(0, 1)$, where a_p and a_s denote the coefficients of compressional and shear wave, respectively. The IOSP for elastic waves can be stated as follows.

Problem 1 (phased IOSP). *Given an incident plane wave $\boldsymbol{u}^{inc}$ for a fixed angular frequency ω, Lamé parameters λ, μ, and a single incident direction d, the IOSP is to determine the location and shape of the boundary Γ_D from the far-field data $(a_p\boldsymbol{v}_p^\infty(\hat{x}), a_s\boldsymbol{v}_s^\infty(\hat{x}))$ $\forall \hat{x} \in \Omega$, which is generated by the obstacle D.*

In the next section, we will show that both the modulus of compressional and shear far-field patterns have translation invariance for a shifted domain, when only the compressional or shear plane wave is used as an incident field. It implies that the inverse problem does not admit a unique solution by using the phaseless far-field patterns. Our goal is to overcome this issue by introducing a reference ball. As seen in Figure 1, an elastically rigid ball $B = \{x \in \mathbb{R}^2 : |x| < R\} \subset \mathbb{R}^2$ with boundary Γ_B is placed next to the obstacle D. The domain B is called the reference ball and is used to break the translation invariance for the far-field pattern. To this end, the phaseless IOSP is stated as follows.

Problem 2 (phaseless IOSP). *Let $B = \{x \in \mathbb{R}^2 : |x| < R\} \subset \mathbb{R}^2$ be an artificially added rigid ball such that $D \cap B = \emptyset$. Given a compressional or shear incident plane wave $\boldsymbol{u}^{inc}$ for a fixed angular frequency ω, Lamé parameters λ, μ, and a single incident direction d, the IOSP is to determine the location and shape of the boundary Γ_D from the phaseless far-field data $(a_p|\boldsymbol{v}_p^\infty(\hat{x})|, a_s|\boldsymbol{v}_s^\infty(\hat{x})|)$ $\forall \hat{x} \in \Omega$, which are generated by the scatterer $D \cup B$.*

In the following, we shall introduce a system of nonlinear integral equations and develop corresponding reconstruction algorithms for solving Problems 1 and 2, respectively.

3. Far-field patterns. In this section, we establish the relationship of the far-field patterns between the scattered field $\boldsymbol{v}$ and the scalar potentials ϕ, ψ.

Denote the fundamental solution to the two-dimensional Helmholtz equation by

$$\Phi(x,y;\kappa)=\frac{\mathrm{i}}{4}H_0^{(1)}(\kappa|x-y|),\quad x\neq y,$$

where $H_0^{(1)}$ is the Hankel function of the first kind with order zero. The following result presents the relation of the far-field patterns of the displacement of the scattered field $\boldsymbol{v}$ and the corresponding scalar potentials ϕ,ψ. Similar results can be found in [4, 13, 14].

Theorem 3.1. *The radiating solution $\boldsymbol{v}$ to the Navier equation has the asymptotic behavior*

$$\boldsymbol{v}(x)=\frac{\mathrm{e}^{\mathrm{i}\kappa_{\mathrm{p}}|x|}}{\sqrt{|x|}}\boldsymbol{v}_{\mathrm{p}}^{\infty}+\frac{\mathrm{e}^{\mathrm{i}\kappa_{\mathrm{s}}|x|}}{\sqrt{|x|}}\boldsymbol{v}_{\mathrm{s}}^{\infty}+\mathcal{O}\left(\frac{1}{|x|^{\frac{3}{2}}}\right),\quad |x|\to\infty,$$

uniformly for all directions $\hat{x}$, where the vectors

$$\boldsymbol{v}_{\mathrm{p}}^{\infty}(\hat{x})=\mathrm{i}\kappa_{\mathrm{p}}\phi_\infty(\hat{x})\hat{x},\qquad \boldsymbol{v}_{\mathrm{s}}^{\infty}(\hat{x})=-\mathrm{i}\kappa_{\mathrm{s}}\psi_\infty(\hat{x})\hat{x}^{\perp}\tag{3.1}$$

defined on the unit circle Ω are the far-field patterns of $\boldsymbol{v}_{\mathrm{p}}$ and $\boldsymbol{v}_{\mathrm{s}}$, and the complex-valued functions $\phi_\infty(\hat{x})$ and $\psi_\infty(\hat{x})$ are the far-field patterns corresponding to ϕ and ψ.

Proof. It follows from Green's formula in [9, Theorem 2.5] that we have

$$\phi(x)=\int_{\Gamma_D}\left\{\phi(y)\frac{\partial\Phi(x,y;\kappa_{\mathrm{p}})}{\partial\nu(y)}-\frac{\partial\phi}{\partial\nu}(y)\Phi(x,y;\kappa_{\mathrm{p}})\right\}\mathrm{d}s(y),\quad x\in\mathbb{R}^2\setminus\overline{D}.$$

The corresponding far-field pattern is

$$\phi_\infty(\hat{x})=\gamma_{\kappa_{\mathrm{p}}}\int_{\Gamma_D}\left\{\phi(y)\frac{\partial\mathrm{e}^{-\mathrm{i}\kappa_{\mathrm{p}}\hat{x}\cdot y}}{\partial\nu(y)}-\frac{\partial\phi}{\partial\nu}(y)\mathrm{e}^{-\mathrm{i}\kappa_{\mathrm{p}}\hat{x}\cdot y}\right\}\mathrm{d}s(y),$$

where $\gamma_{\kappa_{\mathrm{p}}}=\mathrm{e}^{\mathrm{i}\pi/4}/\sqrt{8\kappa_{\mathrm{p}}\pi}$. By the Helmholtz decomposition, the compressional wave can be represented by

$$\boldsymbol{v}_{\mathrm{p}}(x)=\nabla_x\phi(x)=\int_{\Gamma_D}\left\{\phi(y)\frac{\partial}{\partial\nu(y)}\big(\nabla_x\Phi(x,y;\kappa_{\mathrm{p}})\big)-\frac{\partial\phi}{\partial\nu}(y)\nabla_x\Phi(x,y;\kappa_{\mathrm{p}})\right\}\mathrm{d}s(y).\tag{3.2}$$

Using straightforward calculations and noting $H_1^{(1)}=-H_0^{(1)\prime}$, we obtain

$$\nabla_x\Phi(x,y;\kappa_{\mathrm{p}})=\frac{-\mathrm{i}\kappa_{\mathrm{p}}}{4}H_1^{(1)}(\kappa_{\mathrm{p}}|x-y|)\frac{x-y}{|x-y|}.$$

With the help of the asymptotic behavior of the Hankel functions [9, eq. (3.82)]

$$H_n^{(1)}(t)=\sqrt{\frac{2}{\pi t}}\exp\left\{\mathrm{i}\left(t-\frac{n\pi}{2}-\frac{\pi}{4}\right)\right\}\left\{1+\mathcal{O}\left(\frac{1}{t}\right)\right\}$$

and

$$|x-y|=|x|-\hat{x}\cdot y+\mathcal{O}\left(\frac{1}{|x|}\right),$$

we derive

$$\nabla_x \Phi(x,y;\kappa_{\rm p}) = \frac{{\rm e}^{{\rm i}\kappa_{\rm p}|x|}}{\sqrt{|x|}}\left\{ {\rm i}\gamma_{\kappa_{\rm p}}\kappa_{\rm p}{\rm e}^{-{\rm i}\kappa_{\rm p}\hat{x}\cdot y}\hat{x} + \mathcal{O}\left(\frac{1}{|x|}\right)\right\}$$

and

$$\frac{\partial}{\partial\nu(y)}\nabla_x \Phi(x,y;\kappa_{\rm p}) = \frac{{\rm e}^{{\rm i}\kappa_{\rm p}|x|}}{\sqrt{|x|}}\left\{ {\rm i}\gamma_{\kappa_{\rm p}}\kappa_{\rm p}\frac{\partial {\rm e}^{-{\rm i}\kappa_{\rm p}\hat{x}\cdot y}}{\partial\nu(y)}\hat{x} + \mathcal{O}\left(\frac{1}{|x|}\right)\right\}.$$

Substituting the last two equations into (3.2) yields

$$\boldsymbol{v}_{\rm p} = \frac{{\rm e}^{{\rm i}\kappa_{\rm p}|x|}}{\sqrt{|x|}}\left\{ {\rm i}\kappa_{\rm p}\phi_\infty\hat{x} + \mathcal{O}\left(\frac{1}{|x|}\right)\right\}.$$

Similarly, by noting $\boldsymbol{v}_{\rm s} = \mathbf{curl}_x\psi$ and

$$\mathbf{curl}_x \Phi(x,y;\kappa_{\rm s}) = \frac{{\rm i}\kappa_{\rm s}}{4}H_1^{(1)}(\kappa_{\rm s}|x-y|)\frac{(x-y)^\perp}{|x-y|},$$

we obtain that

$$\boldsymbol{v}_{\rm s} = \frac{{\rm e}^{{\rm i}\kappa_{\rm s}|x|}}{\sqrt{|x|}}\left\{ -{\rm i}\kappa_{\rm s}\psi_\infty\hat{x}^\perp + \mathcal{O}\left(\frac{1}{|x|}\right)\right\},$$

which completes the proof. ∎

In view of (3.1), we see that if $(a_{\rm p}\boldsymbol{v}_{\rm p}^\infty, a_{\rm s}\boldsymbol{v}_{\rm s}^\infty)$ or $(a_{\rm p}|\boldsymbol{v}_{\rm p}^\infty|, a_{\rm s}|\boldsymbol{v}_{\rm s}^\infty|)$ is known, then the information on the far-field pattern $(a_{\rm p}\phi_\infty, a_{\rm s}\psi_\infty)$ or $(a_{\rm p}|\phi_\infty|, a_{\rm s}|\psi_\infty|)$ can be obtained. Hence, we may reconstruct the obstacle from the knowledge of $(a_{\rm p}\phi_\infty, a_{\rm s}\psi_\infty)$ and $(a_{\rm p}|\phi_\infty|, a_{\rm s}|\psi_\infty|)$ in Problems 1 and 2, respectively.

The following result show the translation invariance property of the phaseless compressional and shear far-field patterns.

Theorem 3.2. *Assume that ϕ_∞, ψ_∞ are the far-field patterns of the scattered waves ϕ, ψ with incident plane wave $\boldsymbol{u}^{\rm inc}(x) = a_{\rm p}^{\rm inc} d{\rm e}^{{\rm i}\kappa_{\rm p} d\cdot x} + a_{\rm s}^{\rm inc} d^\perp {\rm e}^{{\rm i}\kappa_{\rm s} d\cdot x}$, where $(a_{\rm p}^{\rm inc}, a_{\rm s}^{\rm inc}) = (1,0)$ for the compressional incident plane wave and $(a_{\rm p}^{\rm inc}, a_{\rm s}^{\rm inc}) = (0,1)$ for the shear incident plane wave. For the shifted domain $D_h := \{x + h : x \in D\}$ with a fixed vector $h \in \mathbb{R}^2$, the far-field patterns $\phi_\infty^h, \psi_\infty^h$ satisfy the relations*

$$\phi_\infty^h(\hat{x}) = {\rm e}^{{\rm i}\kappa_{\rm p}(d-\hat{x})\cdot h}\phi_\infty(\hat{x}), \quad \psi_\infty^h(\hat{x}) = {\rm e}^{{\rm i}(\kappa_{\rm p} d - \kappa_{\rm s}\hat{x})\cdot h}\psi_\infty(\hat{x}), \quad (a_{\rm p}^{\rm inc}, a_{\rm s}^{\rm inc}) = (1,0) \tag{3.3}$$

and

$$\psi_\infty^h(\hat{x}) = {\rm e}^{{\rm i}\kappa_{\rm s}(d-\hat{x})\cdot h}\psi_\infty(\hat{x}), \quad \phi_\infty^h(\hat{x}) = {\rm e}^{{\rm i}(\kappa_{\rm s} d - \kappa_{\rm p}\hat{x})\cdot h}\phi_\infty(\hat{x}), \quad (a_{\rm p}^{\rm inc}, a_{\rm s}^{\rm inc}) = (0,1). \tag{3.4}$$

Proof. We only give the proof for the compressional incident plane wave case, i.e., (3.3) for $(a_{\rm p}^{\rm inc}, a_{\rm s}^{\rm inc}) = (1,0)$, since the other case (3.4) for $(a_{\rm p}^{\rm inc}, a_{\rm s}^{\rm inc}) = (0,1)$ can be proved similarly.

We assume that the solution of (2.3) is given as single-layer potentials with densities g_1, g_2:

$$\phi(x) = \int_{\Gamma_D} \Phi(x,y;\kappa_{\rm p})g_1(y){\rm d}s(y), \quad \psi(x) = \int_{\Gamma_D} \Phi(x,y;\kappa_{\rm s})g_2(y){\rm d}s(y), \quad x \in \mathbb{R}^2 \setminus \Gamma_D. \tag{3.5}$$

Letting $x \in \mathbb{R}^2 \setminus \overline{D}$ approach the boundary Γ_D in (3.5), and using the jump relation of single-layer potentials and the boundary condition of (2.3), we deduce for $x \in \Gamma_D$ that

$$-\frac{1}{2}g_1(x) + \int_{\Gamma_D} \frac{\partial \Phi(x,y;\kappa_{\rm p})}{\partial \nu(x)} g_1(y) \mathrm{d}s(y) + \int_{\Gamma_D} \frac{\partial \Phi(x,y;\kappa_{\rm s})}{\partial \tau(x)} g_2(y) \mathrm{d}s(y) = -\nu(x) \cdot \boldsymbol{u}^{\rm inc}(x) \tag{3.6}$$

and

$$\int_{\Gamma_D} \frac{\partial \Phi(x,y;\kappa_{\rm p})}{\partial \tau(x)} g_1(y) \mathrm{d}s(y) + \frac{1}{2}g_2(x) - \int_{\Gamma_D} \frac{\partial \Phi(x,y;\kappa_{\rm s})}{\partial \nu(x)} g_2(y) \mathrm{d}s(y) = -\tau(x) \cdot \boldsymbol{u}^{\rm inc}(x). \tag{3.7}$$

The corresponding far-field patterns can be represented as follows:

$$\phi_\infty(\hat{x}) = \gamma_{\kappa_{\rm p}} \int_{\Gamma_D} \mathrm{e}^{-\mathrm{i}\kappa_{\rm p}\hat{x}\cdot y} g_1(y) \mathrm{d}s(y), \quad \psi_\infty(\hat{x}) = \gamma_{\kappa_{\rm s}} \int_{\Gamma_D} \mathrm{e}^{-\mathrm{i}\kappa_{\rm s}\hat{x}\cdot y} g_2(y) \mathrm{d}s(y), \quad \hat{x} \in \Omega. \tag{3.8}$$

Furthermore, we assume that the densities g_1^h, g_2^h solve the boundary integral equations (3.6)–(3.7) with Γ_D replaced by Γ_{D_h}. We now show that if g_1, g_2 solve (3.6)–(3.7), then

$$g_1^h(x) = \mathrm{e}^{\mathrm{i}\kappa_{\rm p} d\cdot h} g_1(x-h), \qquad g_2^h(x) = \mathrm{e}^{\mathrm{i}\kappa_{\rm p} d\cdot h} g_2(x-h) \tag{3.9}$$

also solve the boundary integral equations (3.6)–(3.7) with Γ_D replaced by Γ_{D_h}. In fact, substituting the above equations into the left side of (3.6)–(3.7) with Γ_D replaced by Γ_{D_h} and setting $\tilde{x} = x - h$, $\tilde{y} = y - h$, we get for $x \in \partial D_h$ that

$$\begin{aligned}
&-\frac{1}{2}g_1^h(x) + \int_{\Gamma_{D_h}} \frac{\partial \Phi(x,y;\kappa_{\rm p})}{\partial \nu(x)} g_1^h(y) \mathrm{d}s(y) + \int_{\Gamma_{D_h}} \frac{\partial \Phi(x,y;\kappa_{\rm s})}{\partial \tau(x)} g_2^h(y) \mathrm{d}s(y) \\
&= \mathrm{e}^{\mathrm{i}\kappa_{\rm p} d\cdot h} \left(-\frac{1}{2}g_1(\tilde{x}) + \int_{\Gamma_D} \frac{\partial \Phi(\tilde{x},\tilde{y};\kappa_{\rm p})}{\partial \nu(\tilde{x})} g_1(\tilde{y}) \mathrm{d}s(\tilde{y}) + \int_{\Gamma_D} \frac{\partial \Phi(\tilde{x},\tilde{y};\kappa_{\rm s})}{\partial \tau(\tilde{x})} g_2(\tilde{y}) \mathrm{d}s(\tilde{y}) \right) \\
&= \mathrm{e}^{\mathrm{i}\kappa_{\rm p} d\cdot h} \big(-\nu(\tilde{x}) \cdot \boldsymbol{u}^{\rm inc}(\tilde{x}) \big) = -\nu(x) \cdot \boldsymbol{u}^{\rm inc}(x).
\end{aligned}$$

Similarly, (3.7) can be handled in the same way. Thus, the relation (3.9) follows from the fact that the system of boundary integral equations (3.6)–(3.7) for D_h has a unique solution [29].

Combining (3.8) and (3.9), we obtain

$$\begin{aligned}
\phi_\infty^h(\hat{x}) &= \gamma_{\kappa_{\rm p}} \int_{\Gamma_{D_h}} \mathrm{e}^{-\mathrm{i}\kappa_{\rm p}\hat{x}\cdot y} g_1^h(y) \mathrm{d}s(y) \\
&= \gamma_{\kappa_{\rm p}} \int_{\Gamma_{D_h}} \mathrm{e}^{-\mathrm{i}\kappa_{\rm p}\hat{x}\cdot(y-h)} \mathrm{e}^{-\mathrm{i}\kappa_{\rm p}\hat{x}\cdot h} \mathrm{e}^{\mathrm{i}\kappa_{\rm p} d\cdot h} g_1(y-h) \mathrm{d}s(y) = \mathrm{e}^{\mathrm{i}\kappa_{\rm p}(d-\hat{x})\cdot h} \phi_\infty(\hat{x})
\end{aligned}$$

and

$$\begin{aligned}
\psi_\infty^h(\hat{x}) &= \gamma_{\kappa_{\rm s}} \int_{\Gamma_{D_h}} \mathrm{e}^{-\mathrm{i}\kappa_{\rm s}\hat{x}\cdot y} g_2^h(y) \mathrm{d}s(y) \\
&= \gamma_{\kappa_{\rm s}} \int_{\Gamma_{D_h}} \mathrm{e}^{-\mathrm{i}\kappa_{\rm s}\hat{x}\cdot(y-h)} \mathrm{e}^{-\mathrm{i}\kappa_{\rm s}\hat{x}\cdot h} \mathrm{e}^{\mathrm{i}\kappa_{\rm p} d\cdot h} g_2(y-h) \mathrm{d}s(y) = \mathrm{e}^{\mathrm{i}(\kappa_{\rm p} d - \kappa_{\rm s}\hat{x})\cdot h} \psi_\infty(\hat{x}),
\end{aligned}$$

which completes the proof. ∎

Theorem 3.2 implies that the modulus of compressional and shear far-field patterns are invariant under translations of the obstacle D for the compressional or shear plane incident wave.

4. Nyström-type discretization for boundary integral equations. In this section, we present a Nyström-type discretization to solve the coupled system (3.6)–(3.7). We first introduce the single-layer integral operator

$$(S_\kappa g)(x) = 2\int_{\Gamma_D} \Phi(x,y;\kappa) g(y) \mathrm{d}s(y), \quad x \in \Gamma_D,$$

and the corresponding far-field integral operator

$$(S_\kappa^\infty g)(\hat{x}) = \gamma_\kappa \int_{\Gamma_D} \mathrm{e}^{-\mathrm{i}\kappa \hat{x}\cdot y} g(y) \mathrm{d}s(y), \quad \hat{x} \in \Omega.$$

In addition, we need to introduce the normal derivative boundary integral operator

$$(K_\kappa g)(x) = 2\int_{\Gamma_D} \frac{\partial \Phi(x,y;\kappa)}{\partial \nu(x)} g(y) \mathrm{d}s(y), \qquad x \in \Gamma_D,$$

and the tangential derivative boundary integral operator

$$(H_\kappa g)(x) = 2\int_{\Gamma_D} \frac{\partial \Phi(x,y;\kappa)}{\partial \tau(x)} g(y) \mathrm{d}s(y), \qquad x \in \Gamma_D.$$

Then, the coupled boundary integral equations (3.6)–(3.7) can be rewritten in the operator form

$$-g_1 + K_{\kappa_\mathrm{p}} g_1 + H_{\kappa_\mathrm{s}} g_2 = 2f_1, \tag{4.1}$$

$$H_{\kappa_\mathrm{p}} g_1 + g_2 - K_{\kappa_\mathrm{s}} g_2 = 2f_2. \tag{4.2}$$

The corresponding far-field patterns of (3.8) can be represented as follows:

$$\phi_\infty(\hat{x}) = (S_{\kappa_\mathrm{p}}^\infty g_1)(\hat{x}), \quad \psi_\infty(\hat{x}) = (S_{\kappa_\mathrm{s}}^\infty g_2)(\hat{x}), \qquad \hat{x} \in \Omega.$$

4.1. Parametrization. For simplicity, the boundary Γ_D is assumed to be a star-shaped curve with the parametric form

$$\Gamma_D = \{p(\hat{x}) = c + r(\hat{x})\hat{x} : \ c = (c_1, c_2)^\top, \ \hat{x} \in \Omega\},$$

where $\Omega = \{\hat{x}(t) = (\cos t, \sin t)^\top : \ 0 \le t < 2\pi\}$. We introduce the parametrized integral operators which are still denoted by S_κ, S_κ^∞, K_κ, and H_κ for convenience, i.e.,

$$\big(S_\kappa(p,\varphi_j)\big)(t) = \frac{\mathrm{i}}{2}\int_0^{2\pi} H_0^{(1)}(\kappa|p(t)-p(\varsigma)|)\varphi_j(\varsigma)\mathrm{d}\varsigma,$$

$$\big(S_\kappa^\infty(p,\varphi_j)\big)(t) = \gamma_\kappa \int_0^{2\pi} \mathrm{e}^{-\mathrm{i}\kappa\hat{x}(t)\cdot p(\varsigma)}\varphi_j(\varsigma)\mathrm{d}\varsigma,$$

$$\big(K_\kappa(p,\varphi_j)\big)(t) = \frac{1}{G(t)}\int_0^{2\pi} \widetilde{K}(t,\varsigma;\kappa)\varphi_j(\varsigma)\mathrm{d}\varsigma,$$

$$\big(H_\kappa(p,\varphi_j)\big)(t) = \frac{1}{G(t)}\int_0^{2\pi} \widetilde{H}(t,\varsigma;\kappa)\varphi_j(\varsigma)\mathrm{d}\varsigma,$$

where $\varphi_j(\varsigma) = G(\varsigma)g_j(p(\varsigma))$, $j = 1, 2$, $G(\varsigma) := |p'(\varsigma)| = \sqrt{(r'(\varsigma))^2 + r^2(\varsigma)}$ is the Jacobian of the transformation,

$$\widetilde{K}(t,\varsigma;\kappa) = \frac{\mathrm{i}\kappa}{2} n(t)\cdot[p(\varsigma)-p(t)]\frac{H_1^{(1)}(\kappa|p(t)-p(\varsigma)|)}{|p(t)-p(\varsigma)|},$$
$$\widetilde{H}(t,\varsigma;\kappa) = \frac{\mathrm{i}\kappa}{2} n(t)^{\perp}\cdot[p(\varsigma)-p(t)]\frac{H_1^{(1)}(\kappa|p(t)-p(\varsigma)|)}{|p(t)-p(\varsigma)|},$$

and

$$n(t) = \nu(p(t))|p'(t)| = \big(p_2'(t), -p_1'(t)\big), \quad n(t)^{\perp} = \tau(p(t))|p'(t)| = \big(p_1'(t), p_2'(t)\big).$$

Hence, (4.1)–(4.2) can be reformulated as the parametrized integral equations

$$-\varphi_1 + K_{\kappa_\mathrm{p}}(p,\varphi_1)G + H_{\kappa_\mathrm{s}}(p,\varphi_2)G = w_1, \tag{4.3}$$
$$\varphi_2 + H_{\kappa_\mathrm{p}}(p,\varphi_1)G - K_{\kappa_\mathrm{s}}(p,\varphi_2)G = w_2, \tag{4.4}$$

where $w_j = 2(f_j \circ p)G$, $j = 1, 2$.

4.2. Discretization. We adopt the Nyström method for the discretization of the boundary integrals. We refer to [24] for an application of the Nyström method to solve the acoustic wave scattering problem by using a hypersingular integral equation.

The kernel $\widetilde{K}$ of the parametrized normal derivative integral operator can be written in the form

$$\widetilde{K}(t,\varsigma;\kappa) = \widetilde{K}_1(t,\varsigma;\kappa)\ln\left(4\sin^2\frac{t-\varsigma}{2}\right) + \widetilde{K}_2(t,\varsigma;\kappa),$$

where

$$\widetilde{K}_1(t,\varsigma;\kappa) = \frac{\kappa}{2\pi} n(t)\cdot\big[p(t)-p(\varsigma)\big]\frac{J_1(\kappa|p(t)-p(\varsigma)|)}{|p(t)-p(\varsigma)|},$$
$$\widetilde{K}_2(t,\varsigma;\kappa) = \widetilde{K}(t,\varsigma;\kappa) - \widetilde{K}_1(t,\varsigma;\kappa)\ln\left(4\sin^2\frac{t-\varsigma}{2}\right).$$

It can be shown that the diagonal terms are

$$\widetilde{K}_1(t,t;\kappa) = 0, \qquad \widetilde{K}_2(t,t;\kappa) = \frac{1}{2\pi}\frac{n(t)\cdot p''(t)}{|p'(t)|^2}.$$

Noting $H_1^{(1)} = J_1 + \mathrm{i}Y_1$, where J_1 and Y_1 are the Bessel and Neumann functions of order one, and using the power series [9, eqs. (3.74) and (3.75)],

$$J_1(z) := \sum_{k=0}^{\infty}\frac{(-1)^k}{k!(k+1)!}\Big(\frac{z}{2}\Big)^{2k+1},$$
$$Y_1(z) := \frac{2}{\pi}\Big\{\ln\frac{z}{2} + C\Big\}J_1(z) - \frac{2}{\pi}\frac{1}{z} - \frac{1}{\pi}\sum_{k=0}^{\infty}\frac{(-1)^k}{k!(k+1)!}\Big\{\psi(k+1)+\psi(k)\Big\}\Big(\frac{z}{2}\Big)^{2k+1},$$

where $\psi(k) = \sum_{m=1}^{k} \frac{1}{m}$ with definition $\psi(0) = 0$ and Euler's constant $C = 0.57721\ldots$, we can split the kernel $\widetilde{H}$ of the parametrized tangential derivative integral operator into

$$\widetilde{H}(t,\varsigma;\kappa) = \widetilde{H}_1(t,\varsigma;\kappa)\frac{1}{\sin(\varsigma - t)} + \widetilde{H}_2(t,\varsigma;\kappa)\ln\left(4\sin^2\frac{t-\varsigma}{2}\right) + \widetilde{H}_3(t,\varsigma;\kappa),$$

where the functions

$$\begin{aligned}
\widetilde{H}_1(t,\varsigma;\kappa) &= \frac{1}{\pi} n(t)^{\perp} \cdot \big[p(\varsigma) - p(t)\big] \frac{\sin(\varsigma - t)}{|p(t) - p(\varsigma)|^2},\\
\widetilde{H}_2(t,\varsigma;\kappa) &= \frac{\kappa}{2\pi} n(t)^{\perp} \cdot \big[p(t) - p(\varsigma)\big] \frac{J_1(\kappa|p(t) - p(\varsigma)|)}{|p(t) - p(\varsigma)|},\\
\widetilde{H}_3(t,\varsigma;\kappa) &= \widetilde{H}(t,\varsigma;\kappa) - \widetilde{H}_1(t,\varsigma;\kappa)\frac{1}{\sin(\varsigma - t)} - \widetilde{H}_2(t,\varsigma;\kappa)\ln\left(4\sin^2\frac{t-\varsigma}{2}\right)
\end{aligned}$$

are analytic with diagonal entries given by

$$\widetilde{H}_1(t,t;\kappa) = \frac{1}{\pi}, \quad \widetilde{H}_2(t,t;\kappa) = 0, \quad \widetilde{H}_3(t,t;\kappa) = 0.$$

Let $\varsigma_j^{(n)} := \pi j/n$, $j = 0,\ldots,2n-1$, be an equidistant set of quadrature points. For the singular integrals, we employ the following quadrature rules via the trigonometric interpolation,

$$\int_0^{2\pi} \ln\left(4\sin^2\frac{t-\varsigma}{2}\right) f(\varsigma)\mathrm{d}\varsigma \approx \sum_{j=0}^{2n-1} R_j^{(n)}(t) f(\varsigma_j^{(n)}), \tag{4.5}$$

$$\int_0^{2\pi} \frac{f(\varsigma)}{\sin(\varsigma - t)}\mathrm{d}\varsigma \approx \sum_{j=0}^{2n-1} T_j^{(n)}(t) f(\varsigma_j^{(n)}), \tag{4.6}$$

where the quadrature weights are given by

$$R_j^{(n)}(t) = -\frac{2\pi}{n}\sum_{m=1}^{n-1}\frac{1}{m}\cos\left[m(t - \varsigma_j^{(n)})\right] - \frac{\pi}{n^2}\cos\left[n(t - \varsigma_j^{(n)})\right] \tag{4.7}$$

and

$$T_j^{(n)}(t) = \begin{cases} -\dfrac{2\pi}{n}\displaystyle\sum_{m=0}^{(n-3)/2} \sin\left[(2m+1)(t - \varsigma_j^{(n)})\right] - \dfrac{\pi}{n}\sin\left[n(t - \varsigma_j^{(n)})\right], & n = 1,3,5,\ldots,\\ -\dfrac{2\pi}{n}\displaystyle\sum_{m=0}^{n/2-1} \sin\left[(2m+1)(t - \varsigma_j^{(n)})\right], & n = 2,4,6,\ldots. \end{cases}$$

Using the Lagrange basis for the trigonometric interpolation [27, eq. (11.12)]), we derive the weight $T_j^{(n)}$ by calculating the integrals

$$\int_0^{2\pi}\frac{\cos k\varsigma}{\sin\varsigma}\mathrm{d}\varsigma = 0, \quad k = 0,1,2,\ldots, \qquad \int_0^{2\pi}\frac{\sin k\varsigma}{\sin\varsigma}\mathrm{d}\varsigma = \begin{cases} 2\pi, & k = 1,3,5\ldots,\\ 0, & k = 2,4,6,\ldots, \end{cases}$$

in the sense of the Cauchy principal value. The details of (4.7) can be found in [27]. For the smooth integrals, we simply use the trapezoidal rule

$$\int_0^{2\pi} f(\varsigma)\mathrm{d}\varsigma \approx \frac{\pi}{n}\sum_{j=0}^{2n-1} f(\varsigma_j^{(n)}). \tag{4.8}$$

By (4.5) and (4.6), the full discretization of (4.3)–(4.4) can be deduced as

$$\begin{aligned} w_{1,i}^{(n)} &= -\varphi_{1,i}^{(n)} + \sum_{j=0}^{2n-1}\left(R_{|i-j|}^{(n)}\widetilde{K}_1(\varsigma_i^{(n)},\varsigma_j^{(n)};\kappa_{\mathrm{p}}) + \frac{\pi}{n}\widetilde{K}_2(\varsigma_i^{(n)},\varsigma_j^{(n)};\kappa_{\mathrm{p}})\right)\varphi_{1,j}^{(n)} \\ &\quad + \sum_{j=0}^{2n-1}\left(-T_{i-j}^{(n)}\widetilde{H}_1(\varsigma_i^{(n)},\varsigma_j^{(n)};\kappa_{\mathrm{s}}) + R_{|i-j|}^{(n)}\widetilde{H}_2(\varsigma_i^{(n)},\varsigma_j^{(n)};\kappa_{\mathrm{s}}) + \frac{\pi}{n}\widetilde{H}_3(\varsigma_i^{(n)},\varsigma_j^{(n)};\kappa_{\mathrm{s}})\right)\varphi_{2,j}^{(n)}, \\ w_{2,i}^{(n)} &= \varphi_{2,i}^{(n)} + \sum_{j=0}^{2n-1}\left(-T_{i-j}^{(n)}\widetilde{H}_1(\varsigma_i^{(n)},\varsigma_j^{(n)};\kappa_{\mathrm{p}}) + R_{|i-j|}^{(n)}H_2(\varsigma_i^{(n)},\varsigma_j^{(n)};\kappa_{\mathrm{p}}) + \frac{\pi}{n}\widetilde{H}_3(\varsigma_i^{(n)},\varsigma_j^{(n)};\kappa_{\mathrm{p}})\right)\varphi_{1,j}^{(n)} \\ &\quad - \sum_{j=0}^{2n-1}\left(R_{|i-j|}^{(n)}\widetilde{K}_1(\varsigma_i^{(n)},\varsigma_j^{(n)};\kappa_{\mathrm{s}}) + \frac{\pi}{n}\widetilde{K}_2(\varsigma_i^{(n)},\varsigma_j^{(n)};\kappa_{\mathrm{s}})\right)\varphi_{2,j}^{(n)}, \end{aligned}$$

where $w_{l,i}^{(n)} = w_l(\varsigma_i^{(n)})$, $\varphi_{l,j}^{(n)} = \varphi_l(\varsigma_j^{(n)})$ for $i,j = 0,\dots,2n-1$, $l = 1,2$, and

$$R_j^{(n)} := R_j^{(n)}(0) = -\frac{2\pi}{n}\sum_{m=1}^{n-1}\frac{1}{m}\cos\frac{mj\pi}{n} - \frac{(-1)^j\pi}{n^2},$$

$$T_j^{(n)} := T_j^{(n)}(0) = \frac{2\pi}{n}\sum_{m=0}^{\tilde{n}}\sin\frac{(2m+1)j\pi}{n}, \qquad \tilde{n} = \begin{cases}(n-3)/2, & n = 1,3,5,\dots,\\ n/2-1, & n = 2,4,6,\dots.\end{cases}$$

5. Reconstruction methods. In this section, we introduce a system of nonlinear equations and develop corresponding reconstruction methods for Problems 1 and 2, respectively.

5.1. The phased IOSP. On Γ_D, it follows from the boundary integral equations (4.1)–(4.2) that the field equations are

$$-g_1 + K_{\kappa_{\mathrm{p}}}g_1 + H_{\kappa_{\mathrm{s}}}g_2 = 2f_1, \tag{5.1}$$

$$H_{\kappa_{\mathrm{p}}}g_1 + g_2 - K_{\kappa_{\mathrm{s}}}g_2 = 2f_2. \tag{5.2}$$

The data equation is given by

$$a_{\mathrm{p}}S_{\kappa_{\mathrm{p}}}^{\infty}g_1 + a_{\mathrm{s}}S_{\kappa_{\mathrm{s}}}^{\infty}g_2 = a_{\mathrm{p}}\phi_\infty + a_{\mathrm{s}}\psi_\infty. \tag{5.3}$$

The field equations and data equation (5.1)–(5.3) can be reformulated as the parametrized integral equations

$$-\varphi_1 + K_{\kappa_{\mathrm{p}}}(p,\varphi_1)G + H_{\kappa_{\mathrm{s}}}(p,\varphi_2)G = w_1, \tag{5.4}$$

$$\varphi_2 + H_{\kappa_{\mathrm{p}}}(p,\varphi_1)G - K_{\kappa_{\mathrm{s}}}(p,\varphi_2)G = w_2, \tag{5.5}$$

$$a_{\mathrm{p}}S_{\kappa_{\mathrm{p}}}^{\infty}(p,\varphi_1) + a_{\mathrm{s}}S_{\kappa_{\mathrm{s}}}^{\infty}(p,\varphi_2) = a_{\mathrm{p}}\phi_\infty + a_{\mathrm{s}}\psi_\infty, \tag{5.6}$$

where $w_j = 2(f_j\circ p)G$, $j = 1,2$.

In the reconstruction process, when an approximation of the boundary Γ_D is available, the field equations (5.4)–(5.5) are solved for the densities φ_1 and φ_2. Once the approximated densities φ_1 and φ_2 are computed, the update of the boundary Γ_D can be obtained by solving the linearized data equation (5.6) with respect to Γ_D.

5.1.1. Iterative scheme. The linearization of (5.6) with respect to p requires the Fréchet derivative of the parametrized integral operator S_κ^∞, which can be explicitly calculated as follows:

$$\begin{aligned}\Big(S_\kappa^{\infty\prime}[p;\varphi]q\Big)(t) &= -\mathrm{i}\kappa\gamma_\kappa \int_0^{2\pi} \mathrm{e}^{-\mathrm{i}\kappa\hat{x}(t)\cdot p(\varsigma)}\hat{x}(t)\cdot q(\varsigma)\varphi(\varsigma)\mathrm{d}\varsigma \\ &= -\mathrm{i}\kappa\gamma_\kappa \int_0^{2\pi} \exp\Big(-\mathrm{i}\kappa\big(c_1\cos t + c_2\sin t + r(\varsigma)\cos(t-\varsigma)\big)\Big) \\ &\quad \times \Big(\Delta c_1\cos t + \Delta c_2\sin t + \Delta r(\varsigma)\cos(t-\varsigma)\Big)\varphi(\varsigma)\,\mathrm{d}\varsigma, \end{aligned} \tag{5.7}$$

where

$$q(\varsigma) = (\Delta c_1, \Delta c_2) + \Delta r(\varsigma)(\cos\varsigma, \sin\varsigma)$$

gives the update of the boundary Γ_D. Then, the linearization of (5.6) leads to

$$a_{\mathrm{p}} S_{\kappa_{\mathrm{p}}}^{\infty\prime}[p;\varphi_1]q + a_{\mathrm{s}} S_{\kappa_{\mathrm{s}}}^{\infty\prime}[p;\varphi_2]q = w, \tag{5.8}$$

where

$$w := a_{\mathrm{p}}\Big(\phi_\infty - S_{\kappa_{\mathrm{p}}}^\infty(p,\varphi_1)\Big) + a_{\mathrm{s}}\Big(\psi_\infty - S_{\kappa_{\mathrm{s}}}^\infty(p,\varphi_2)\Big).$$

As usual, a stopping criterion is necessary to terminate the iteration. For our iterative procedure, the following relative error estimator is used:

$$\mathrm{E}_k := \frac{\Big\|a_{\mathrm{p}}\Big(\phi_\infty - S_{\kappa_{\mathrm{p}}}^\infty(p^{(k)},\varphi_1)\Big) + a_{\mathrm{s}}\Big(\psi_\infty - S_{\kappa_{\mathrm{s}}}^\infty(p^{(k)},\varphi_2)\Big)\Big\|_{L^2}}{\big\|a_{\mathrm{p}}\phi_\infty + a_{\mathrm{s}}\psi_\infty\big\|_{L^2}} \le \epsilon, \tag{5.9}$$

where ϵ is a user-specified small positive constant depending on the noise level and $p^{(k)}$ is the kth approximation of the boundary Γ_D.

We are now in a position to present the iterative algorithm Algorithm 1 for the ISOP with phased far-field data.

5.1.2. Discretization. We use the Nyström method which is described in section 4 for the full discretizations of (5.4)–(5.5). Now we discuss the discretization of the linearized equation (5.8) and obtain the update by using least squares with Tikhonov regularization [26]. As for a finite-dimensional space to approximate the radial function r and its update Δr, we choose the space of trigonometric polynomials of the form

$$\Delta r(\varsigma) = \sum_{m=0}^{M} \alpha_m \cos m\varsigma + \sum_{m=1}^{M} \beta_m \sin m\varsigma, \tag{5.10}$$

Algorithm 1 Iterative algorithm for the phased IOSP.

Step 1	Send an incident plane wave $\boldsymbol{u}^{\text{inc}}$ with fixed ω, λ, μ, and a fixed incident direction $d \in \Omega$, and then collect the corresponding far-field data ϕ_∞ or ψ_∞ for the scatterer D.
Step 2	Select an initial starlike curve $\Gamma^{(0)}$ for the boundary Γ_D and the error tolerance ϵ. Set $k = 0$.
Step 3	For the curve $\Gamma^{(k)}$, compute the densities φ_1 and φ_2 from (5.4)–(5.5).
Step 4	Solve (5.8) to obtain the updated approximation $\Gamma^{(k+1)} := \Gamma^{(k)} + q$ and evaluate the error E_{k+1} defined in (5.9).
Step 5	If $E_{k+1} \geq \epsilon$, then set $k = k + 1$ and go to Step 3. Otherwise, the current approximation $\Gamma^{(k+1)}$ is taken to be the final reconstruction of Γ_D.

where the integer $M > 1$ denotes the truncation number. For simplicity, we reformulate equation (5.8) by introducing the following definitions:

$$
\begin{aligned}
L_1(t,\varsigma;\kappa,\varphi) &:= -\mathrm{i}\kappa\gamma_\kappa \exp\left\{-\mathrm{i}\kappa\Big(c_1\cos t + c_2 \sin t + r(\varsigma)\cos(t-\varsigma)\Big)\right\}\cos t\ \varphi(\varsigma),\\
L_2(t,\varsigma;\kappa,\varphi) &:= -\mathrm{i}\kappa\gamma_\kappa \exp\left\{-\mathrm{i}\kappa\Big(c_1\cos t + c_2 \sin t + r(\varsigma)\cos(t-\varsigma)\Big)\right\}\sin t\ \varphi(\varsigma),\\
L_{3,m}(t,\varsigma;\kappa,\varphi) &:= -\mathrm{i}\kappa\gamma_\kappa \exp\left\{-\mathrm{i}\kappa\Big(c_1\cos t + c_2 \sin t + r(\varsigma)\cos(t-\varsigma)\Big)\right\}\cos(t-\varsigma)\cos m\varsigma\ \varphi(\varsigma),\\
L_{4,m}(t,\varsigma;\kappa,\varphi) &:= -\mathrm{i}\kappa\gamma_\kappa \exp\left\{-\mathrm{i}\kappa\Big(c_1\cos t + c_2 \sin t + r(\varsigma)\cos(t-\varsigma)\Big)\right\}\cos(t-\varsigma)\sin m\varsigma\ \varphi(\varsigma).
\end{aligned}
$$

Combining (5.7)–(5.8) and using the trapezoidal rule (4.8), we get the discretized linear system

$$
\begin{aligned}
&a_{\mathrm{p}}\left(\sum_{l=1}^{2} B_l^c(\varsigma_i^{(\bar{n})};\kappa_{\mathrm{p}},\varphi_1)\Delta c_l + \sum_{m=0}^{M}\alpha_m B_{1,m}^r(\varsigma_i^{(\bar{n})};\kappa_{\mathrm{p}},\varphi_1) + \sum_{m=1}^{M}\beta_m B_{2,m}^r(\varsigma_i^{(\bar{n})};\kappa_{\mathrm{p}},\varphi_1)\right)\\
&\quad + a_{\mathrm{s}}\left(\sum_{l=1}^{2} B_j^c(\varsigma_i^{(\bar{n})};\kappa_{\mathrm{s}},\varphi_2)\Delta c_l + \sum_{m=0}^{M}\alpha_m B_{1,m}^r(\varsigma_i^{(\bar{n})};\kappa_{\mathrm{s}},\varphi_2) + \sum_{m=1}^{M}\beta_m B_{2,m}^r(\varsigma_i^{(\bar{n})};\kappa_{\mathrm{s}},\varphi_2)\right)\\
&\qquad = w(\varsigma_i^{(\bar{n})})
\end{aligned}
\tag{5.11}
$$

to determine the real coefficients Δc_1, Δc_2, α_m, and β_m, where

$$
B_l^c(\varsigma_i^{(\bar{n})};\kappa,\varphi) = \frac{\pi}{n}\sum_{j=0}^{2n-1} L_l(\varsigma_i^{(\bar{n})},\varsigma_j^{(n)};\kappa,\varphi), \quad l = 1,2,
$$

and

$$
\begin{aligned}
B_{1,m}^r(\varsigma_i^{(\bar{n})};\kappa,\varphi) &= \frac{\pi}{n}\sum_{j=0}^{2n-1} L_{3,m}(\varsigma_i^{(\bar{n})},\varsigma_j^{(n)};\kappa,\varphi),\\
B_{2,m}^r(\varsigma_i^{(\bar{n})};\kappa,\varphi) &= \frac{\pi}{n}\sum_{j=0}^{2n-1} L_{4,m}(\varsigma_i^{(\bar{n})},\varsigma_j^{(n)};\kappa,\varphi).
\end{aligned}
$$

In general, $2M+1 \ll 2\bar{n}$, and due to the ill-posedness, the overdetermined system (5.11) is solved via the Tikhonov regularization. Hence the linear system (5.11) is reformulated into minimizing the following function:

$$\sum_{i=0}^{2\bar{n}-1} \Bigg| a_{\mathrm{p}} \left(\sum_{l=1}^{2} B_l^c(\varsigma_i^{(\bar{n})}; \kappa_{\mathrm{p}}, \varphi_1)\Delta c_l + \sum_{m=0}^{M} \alpha_m B_{1,m}^r(\varsigma_i^{(\bar{n})}; \kappa_{\mathrm{p}}, \varphi_1) + \sum_{m=1}^{M} \beta_m B_{2,m}^r(\varsigma_i^{(\bar{n})}; \kappa_{\mathrm{p}}, \varphi_1) \right) + a_{\mathrm{s}} \left(\sum_{l=1}^{2} B_j^c(\varsigma_i^{(\bar{n})}; \kappa_{\mathrm{s}}, \varphi_2)\Delta c_l + \sum_{m=0}^{M} \alpha_m B_{1,m}^r(\varsigma_i^{(\bar{n})}; \kappa_{\mathrm{s}}, \varphi_2) + \sum_{m=1}^{M} \beta_m B_{2,m}^r(\varsigma_i^{(\bar{n})}; \kappa_{\mathrm{s}}, \varphi_2) \right) - w(\varsigma_i^{(\bar{n})}) \Bigg|^2 + \lambda \left(|\Delta c_1|^2 + |\Delta c_2|^2 + 2\pi \left[\alpha_0^2 + \frac{1}{2} \sum_{m=1}^{M} (1+m^2)^2 (\alpha_m^2 + \beta_m^2) \right] \right), \tag{5.12}$$

where $\lambda > 0$ is a regularization parameter. It is easy to show that the minimizer of (5.12) is the solution of the system

$$\lambda \widetilde{I}\xi + \Re(\widetilde{B}^* \widetilde{B})\xi = \Re(\widetilde{B}^* \widetilde{w}), \tag{5.13}$$

where

$$\begin{aligned} \widetilde{B} = \Big(& a_{\mathrm{p}} B_1^c(:, \kappa_{\mathrm{p}}, \varphi_1) + a_{\mathrm{s}} B_1^c(:, \kappa_{\mathrm{s}}, \varphi_2), a_{\mathrm{p}} B_2^c(:, \kappa_{\mathrm{p}}, \varphi_1) + a_{\mathrm{s}} B_2^c(:, \kappa_{\mathrm{s}}, \varphi_2), \\ & a_{\mathrm{p}} B_{1,0}^r(:, \kappa_{\mathrm{p}}, \varphi_1) + a_{\mathrm{s}} B_{1,0}^r(:, \kappa_{\mathrm{s}}, \varphi_2), \ldots, a_{\mathrm{p}} B_{1,M}^r(:, \kappa_{\mathrm{p}}, \varphi_1) + a_{\mathrm{s}} B_{1,M}^r(:, \kappa_{\mathrm{s}}, \varphi_2), \\ & a_{\mathrm{p}} B_{2,1}^r(:, \kappa_{\mathrm{p}}, \varphi_1) + a_{\mathrm{s}} B_{2,1}^r(:, \kappa_{\mathrm{s}}, \varphi_2), \ldots, a_{\mathrm{p}} B_{2,M}^r(:, \kappa_{\mathrm{p}}, \varphi_1) + a_{\mathrm{s}} B_{2,M}^r(:, \kappa_{\mathrm{s}}, \varphi_2) \Big)_{(2\bar{n}) \times (2M+3)} \end{aligned}$$

and

$$\begin{aligned} & \xi = (\Delta c_1, \Delta c_2, \alpha_0, \ldots, \alpha_M, \beta_1, \ldots, \beta_M)^\top, \\ & \widetilde{I} = \mathrm{diag}\{1, 1, 2\pi, \pi(1+1^2)^2, \ldots, \pi(1+M^2)^2, \pi(1+1^2)^2, \ldots, \pi(1+M^2)^2\}, \\ & \widetilde{w} = (w(\varsigma_0^{(\bar{n})}), \ldots, w(\varsigma_{2\bar{n}-1}^{(\bar{n})}))^\top. \end{aligned}$$

Thus, we obtain the new approximation

$$p^{new}(\hat{x}) = (c + \Delta c) + \big(r(\hat{x}) + \Delta r(\hat{x})\big)\hat{x}.$$

5.2. The phaseless IOSP. To incorporate the reference ball, we find the solution of (2.3) with D replaced by $D \cup B$ in the form of single-layer potentials with densities $g_{1,\sigma}$ and $g_{2,\sigma}$:

$$\phi(x) = \sum_{\sigma} \int_{\Gamma_\sigma} \Phi(x, y; \kappa_{\mathrm{p}}) g_{1,\sigma}(y) \mathrm{d}s(y), \quad \psi(x) = \sum_{\sigma} \int_{\Gamma_\sigma} \Phi(x, y; \kappa_{\mathrm{s}}) g_{2,\sigma}(y) \mathrm{d}s(y) \tag{5.14}$$

for $x \in \mathbb{R}^2 \setminus \Gamma_{D \cup B}$, where $\sigma = D, B$. We introduce integral operators

$$\begin{aligned} (K_\kappa^{\sigma,\varrho} g)(x) &= 2 \int_{\Gamma_\sigma} \frac{\partial \Phi(x, y; \kappa)}{\partial \nu(x)} g(y) \mathrm{d}s(y), \quad x \in \Gamma_\varrho, \\ (H_\kappa^{\sigma,\varrho} g)(x) &= 2 \int_{\Gamma_\sigma} \frac{\partial \Phi(x, y; \kappa)}{\partial \tau(x)} g(y) \mathrm{d}s(y), \quad x \in \Gamma_\varrho, \end{aligned}$$

and the corresponding far-field pattern

$$(S^{\infty}_{\kappa,\sigma}g)(\hat{x}) = \gamma_\kappa \int_{\Gamma_\sigma} \mathrm{e}^{-\mathrm{i}\kappa\hat{x}\cdot y} g(y)\mathrm{d}s(y), \quad \hat{x}\in\Omega,$$

where $\varrho = D, B$. Letting $x \in \mathbb{R}^2 \setminus \overline{D \cup B}$ approach the boundary Γ_D and Γ_B, respectively, in (5.14), and using the jump relation of single-layer potentials and the boundary condition of (2.3) for $\Gamma_D \cup \Gamma_B$, we deduce the field equations in the operator form:

$$-g_{1,D} + \sum_\sigma K^{\sigma,D}_{\kappa_\mathrm{p}} g_{1,\sigma} + \sum_\sigma H^{\sigma,D}_{\kappa_\mathrm{s}} g_{2,\sigma} = 2f_1 \quad \text{on } \Gamma_D, \tag{5.15}$$

$$g_{2,D} + \sum_\sigma H^{\sigma,D}_{\kappa_\mathrm{p}} g_{1,\sigma} - \sum_\sigma K^{\sigma,D}_{\kappa_\mathrm{s}} g_{2,\sigma} = 2f_2 \quad \text{on } \Gamma_D, \tag{5.16}$$

$$-g_{1,B} + \sum_\sigma K^{\sigma,B}_{\kappa_\mathrm{p}} g_{1,\sigma} + \sum_\sigma H^{\sigma,B}_{\kappa_\mathrm{s}} g_{2,\sigma} = 2f_1 \quad \text{on } \Gamma_B, \tag{5.17}$$

$$g_{2,B} + \sum_\sigma H^{\sigma,B}_{\kappa_\mathrm{p}} g_{1,\sigma} - \sum_\sigma K^{\sigma,B}_{\kappa_\mathrm{s}} g_{2,\sigma} = 2f_2 \quad \text{on } \Gamma_B. \tag{5.18}$$

The phaseless data equation can be written as

$$a_\mathrm{p}\left|\sum_\sigma S^{\infty}_{\kappa_\mathrm{p},\sigma} g_{1,\sigma}\right|^2 + a_\mathrm{s}\left|\sum_\sigma S^{\infty}_{\kappa_\mathrm{s},\sigma} g_{2,\sigma}\right|^2 = a_\mathrm{p}|\phi_\infty|^2 + a_\mathrm{s}|\psi_\infty|^2. \tag{5.19}$$

In the reconstruction process, for a given approximated boundary Γ_D, the field equations (5.15)–(5.18) can be solved for the densities $g_{1,\sigma}$ and $g_{2,\sigma}$. Once $g_{1,\sigma}$ and $g_{2,\sigma}$ are computed, the update of the boundary Γ_D can be obtained by linearizing (5.19) with respect to Γ_D.

5.2.1. Parametrization and iterative scheme. For simplicity, the boundary Γ_D and Γ_B are assumed to be star-shaped curves with the parametric forms

$$\Gamma_D = \{p_D(\hat{x}) = c + r(\hat{x})\hat{x} : \ c = (c_1, c_2)^\top, \ \hat{x}\in\Omega\},$$
$$\Gamma_B = \{p_B(\hat{x}) = b + R\hat{x} : \ b = (b_1, b_2)^\top, \ \hat{x}\in\Omega\},$$

where $\Omega = \{\hat{x}(t) = (\cos t, \sin t)^\top : \ 0 \le t < 2\pi\}$. Using the parametric forms of the boundaries Γ_D and Γ_B, we introduce the parametrized integral operators which are still represented by S_κ, S^∞_κ, K_κ, and H_κ for convenience, i.e.,

$$\big(S^{\sigma,\varrho}_\kappa \varphi_{j,\sigma}\big)(t) = \frac{\mathrm{i}}{2}\int_0^{2\pi} H^{(1)}_0(\kappa|p_\varrho(t) - p_\sigma(\varsigma)|)\varphi_{j,\sigma}(\varsigma)\mathrm{d}\varsigma,$$
$$\big(S^\infty_\kappa(p,\varphi_{j,\sigma})\big)(t) = \gamma_\kappa \int_0^{2\pi} \mathrm{e}^{-\mathrm{i}\kappa\hat{x}(t)\cdot p(\varsigma)}\varphi_{j,\sigma}(\varsigma)\mathrm{d}\varsigma,$$
$$\big(K^{\sigma,\varrho}_\kappa \varphi_{j,\sigma}\big)(t) = \frac{1}{G_\varrho(t)}\int_0^{2\pi} \widetilde{K}^{\sigma,\varrho}(t,\varsigma;\kappa)\varphi_{j,\sigma}(\varsigma)\mathrm{d}\varsigma,$$
$$\big(H^{\sigma,\varrho}_\kappa \varphi_{j,\sigma}\big)(t) = \frac{1}{G_\varrho(t)}\int_0^{2\pi} \widetilde{H}^{\sigma,\varrho}(t,\varsigma;\kappa)\varphi_{j,\sigma}(\varsigma)\mathrm{d}\varsigma,$$

where the integral kernels are

$$\widetilde{K}^{\sigma,\varrho}(t,\varsigma;\kappa)=\frac{\mathrm{i}\kappa}{2}n_\varrho(t)\cdot[p_\sigma(\varsigma)-p_\varrho(t)]\frac{H_1^{(1)}(\kappa|p_\varrho(t)-p_\sigma(\varsigma)|)}{|p_\varrho(t)-p_\sigma(\varsigma)|},$$
$$\widetilde{H}^{\sigma,\varrho}(t,\varsigma;\kappa)=\frac{\mathrm{i}\kappa}{2}n_\varrho(t)^\perp\cdot[p_\sigma(\varsigma)-p_\varrho(t)]\frac{H_1^{(1)}(\kappa|p_\varrho(t)-p_\sigma(\varsigma)|)}{|p_\varrho(t)-p_\sigma(\varsigma)|}.$$

Here $\varphi_{j,\sigma}(\varsigma)=G_\sigma(\varsigma)g_j(p_\sigma(\varsigma))$, $j=1,2$, $\sigma=D,B$, where $G_D(\varsigma):=|p_D'(\varsigma)|=\sqrt{(r'(\varsigma))^2+r^2(\varsigma)}$ and $G_B=R$ are the Jacobians of the transformation, and

$$n_\varrho(t)=\nu(p_\varrho(t))|p_\varrho'(t)|=\big(p_{2,\varrho}'(t),-p_{1,\varrho}'(t)\big),$$
$$n_\varrho(t)^\perp=\tau(p_\varrho(t))|p_\varrho'(t)|=\big(p_{1,\varrho}'(t),p_{2,\varrho}'(t)\big).$$

The field equations (5.15)–(5.18) can be reformulated as the parametrized integral equations

(5.20)
$$-\varphi_{1,D}+(K_{\kappa_\mathrm{p}}^{D,D}\varphi_{1,D})G_D+(K_{\kappa_\mathrm{p}}^{B,D}\varphi_{1,B})G_D+(H_{\kappa_\mathrm{s}}^{D,D}\varphi_{2,D})G_D+(H_{\kappa_\mathrm{s}}^{B,D}\varphi_{2,B})G_D=w_{1,D},$$

(5.21)
$$\varphi_{2,D}+(H_{\kappa_\mathrm{p}}^{D,D}\varphi_{1,D})G_D+(H_{\kappa_\mathrm{p}}^{B,D}\varphi_{1,B})G_D-(K_{\kappa_\mathrm{s}}^{D,D}\varphi_{2,D})G_D-(K_{\kappa_\mathrm{s}}^{B,D}\varphi_{2,B})G_D=w_{2,D},$$

(5.22)
$$-\varphi_{1,B}+(K_{\kappa_\mathrm{p}}^{D,B}\varphi_{1,D})G_B+(K_{\kappa_\mathrm{p}}^{B,B}\varphi_{1,B})G_B+(H_{\kappa_\mathrm{s}}^{D,B}\varphi_{2,D})G_B+(H_{\kappa_\mathrm{s}}^{B,B}\varphi_{2,B})G_B=w_{1,B},$$

(5.23)
$$\varphi_{2,B}+(H_{\kappa_\mathrm{p}}^{D,B}\varphi_{1,D})G_B+(H_{\kappa_\mathrm{p}}^{B,B}\varphi_{1,B})G_B-(K_{\kappa_\mathrm{s}}^{D,B}\varphi_{2,D})G_B-(K_{\kappa_\mathrm{s}}^{B,B}\varphi_{2,B})G_B=w_{2,B},$$

and the phaseless data equation (5.19) can be written as

(5.24)
$$a_\mathrm{p}\bigg|\sum_\sigma S_{\kappa_\mathrm{p}}^\infty(p_\sigma,\varphi_{1,\sigma})\bigg|^2+a_\mathrm{s}\bigg|\sum_\sigma S_{\kappa_\mathrm{s}}^\infty(p_\sigma,\varphi_{2,\sigma})\bigg|^2=a_\mathrm{p}|\phi_\infty|^2+a_\mathrm{s}|\psi_\infty|^2.$$

with $w_{j,\sigma}=2(f_j\circ p_\sigma)G_\sigma$, $j=1,2$, $\sigma=D,B$.

It follows from the Fréchet derivative operator $S_\kappa^{\infty\prime}[p;\varphi]q$ in (5.7) that the linearization of (5.24) leads to

(5.25)
$$a_\mathrm{p}2\Re\left(\overline{\sum_\sigma S_{\kappa_\mathrm{p}}^\infty(p_\sigma,\varphi_{1,\sigma})}S_{\kappa_\mathrm{p}}^{\infty\prime}[p_D;\varphi_{1,D}]q\right)+a_\mathrm{s}2\Re\left(\overline{\sum_\sigma S_{\kappa_\mathrm{s}}^\infty(p_\sigma,\varphi_{2,\sigma})}S_{\kappa_\mathrm{s}}^{\infty\prime}[p_D;\varphi_{2,D}]q\right)=\breve{w},$$

where

$$\breve{w}:=a_\mathrm{p}\left(|\phi_\infty|^2-\bigg|\sum_\sigma S_{\kappa_\mathrm{p}}^\infty(p_\sigma,\varphi_{1,\sigma})\bigg|^2\right)+a_\mathrm{s}\left(|\psi_\infty|^2-\bigg|\sum_\sigma S_{\kappa_\mathrm{s}}^\infty(p_\sigma,\varphi_{2,\sigma})\bigg|^2\right).$$

Again, we may choose the following relative error estimator to terminate the iteration,

(5.26)
$$\mathrm{E}_k:=\frac{\|a_\mathrm{p}\phi_k+a_\mathrm{s}\psi_k\|_{L^2}}{\big\|a_\mathrm{p}|\phi_\infty|^2+a_\mathrm{s}|\psi_\infty|^2\big\|_{L^2}}\le\epsilon,$$

where $\epsilon>0$ is the tolerance parameter which depends on the noise level and $p_D^{(k)}$ is the kth

approximation of the boundary Γ_D and

$$\phi_k = |\phi_\infty|^2 - \left|S^\infty_{\kappa_\mathrm{p}}(p_D^{(k)}, \varphi_{1,D}) + S^\infty_{\kappa_\mathrm{p}}(p_B, \varphi_{1,B})\right|^2,$$
$$\psi_k = |\psi_\infty|^2 - \left|S^\infty_{\kappa_\mathrm{s}}(p_D^{(k)}, \varphi_{2,D}) + S^\infty_{\kappa_\mathrm{s}}(p_B, \varphi_{2,B})\right|^2.$$

The iterative algorithm for the phaseless IOSP is given by Algorithm 2.

Algorithm 2 Iterative algorithm for the phaseless IOSP.

Step 1	Send an incident plane wave $\boldsymbol{u}^{\mathrm{inc}}$ with fixed ω, λ, μ and a fixed incident direction $d \in \Omega$, and then collect the corresponding phaseless far-field data $\|\phi_\infty\|$ or $\|\psi_\infty\|$ for the scatterer $D \cup B$.
Step 2	Select an initial starlike curve $\Gamma^{(0)}$ for the boundary Γ_D and the error tolerance ϵ. Set $k = 0$.
Step 3	For the curve $\Gamma^{(k)}$, compute the densities $\varphi_{1,\sigma}$ and $\varphi_{2,\sigma}$ from (5.20)–(5.23).
Step 4	Solve (5.25) to obtain the updated approximation $\Gamma^{(k+1)} := \Gamma^{(k)} + q$ and evaluate the error E_{k+1} defined in (5.26).
Step 5	If $E_{k+1} \geq \epsilon$, then set $k = k + 1$ and go to Step 3. Otherwise, the current approximation $\Gamma^{(k+1)}$ is served as the final reconstruction of Γ_D.

5.2.2. Discretization. We point out that the kernels $\widetilde{K}^{\sigma,\varrho}$ and $\widetilde{H}^{\sigma,\varrho}$ are singular when $\sigma = \varrho$. By the quadrature rules (4.5)–(4.6), the full discretization of (5.20)–(5.23) can be deduced as follows:

$$\begin{aligned}
w_{1,D}^{(n),i} =& -\varphi_{1,D}^{(n),i} + \sum_{j=0}^{2n-1}\left(R^{(n)}_{|i-j|}\widetilde{K}_1^{D,D}(\varsigma_i^{(n)},\varsigma_j^{(n)};\kappa_\mathrm{p}) + \frac{\pi}{n}\widetilde{K}_2^{D,D}(\varsigma_i^{(n)},\varsigma_j^{(n)};\kappa_\mathrm{p})\right)\varphi_{1,D}^{(n),j}\\
&+\sum_{j=0}^{2n-1}\frac{\pi}{n}\widetilde{K}^{B,D}(\varsigma_i^{(n)},\varsigma_j^{(n)};\kappa_\mathrm{p})\varphi_{1,B}^{(n),j} + \sum_{j=0}^{2n-1}\frac{\pi}{n}\widetilde{H}^{B,D}(\varsigma_i^{(n)},\varsigma_j^{(n)};\kappa_\mathrm{s})\varphi_{2,B}^{(n),j}\\
&+\sum_{j=0}^{2n-1}\left(-T^{(n)}_{i-j}\widetilde{H}_1^{D,D}(\varsigma_i^{(n)},\varsigma_j^{(n)};\kappa_\mathrm{s}) + R^{(n)}_{|i-j|}\widetilde{H}_2^{D,D}(\varsigma_i^{(n)},\varsigma_j^{(n)};\kappa_\mathrm{s}) + \frac{\pi}{n}\widetilde{H}_3^{D,D}(\varsigma_i^{(n)},\varsigma_j^{(n)};\kappa_\mathrm{s})\right)\varphi_{2,D}^{(n),j},\\
w_{2,D}^{(n),i} =& \varphi_{2,D}^{(n),i} + \sum_{j=0}^{2n-1}\left(-T^{(n)}_{i-j}\widetilde{H}_1^{D,D}(\varsigma_i^{(n)},\varsigma_j^{(n)};\kappa_\mathrm{p}) + R^{(n)}_{|i-j|}\widetilde{H}_2^{D,D}(\varsigma_i^{(n)},\varsigma_j^{(n)};\kappa_\mathrm{p})\right.\\
&\qquad\left.+\frac{\pi}{n}\widetilde{H}_3^{D,D}(\varsigma_i^{(n)},\varsigma_j^{(n)};\kappa_\mathrm{p})\right)\varphi_{1,D}^{(n),j}\\
&+\sum_{j=0}^{2n-1}\frac{\pi}{n}\widetilde{H}^{B,D}(\varsigma_i^{(n)},\varsigma_j^{(n)};\kappa_\mathrm{p})\varphi_{1,B}^{(n),j}\\
&-\sum_{j=0}^{2n-1}\left(R^{(n)}_{|i-j|}\widetilde{K}_1^{D,D}(\varsigma_i^{(n)},\varsigma_j^{(n)};\kappa_\mathrm{s}) + \frac{\pi}{n}\widetilde{K}_2^{D,D}(\varsigma_i^{(n)},\varsigma_j^{(n)};\kappa_\mathrm{s})\right)\varphi_{2,D}^{(n),j}\\
&-\sum_{j=0}^{2n-1}\frac{\pi}{n}\widetilde{K}^{B,D}(\varsigma_i^{(n)},\varsigma_j^{(n)};\kappa_\mathrm{s})\varphi_{2,B}^{(n),j},
\end{aligned}$$

$$
\begin{aligned}
w_{1,B}^{(n),i} = & -\varphi_{1,B}^{(n),i} + \sum_{j=0}^{2n-1} \frac{\pi}{n} \widetilde{K}^{D,B}(\varsigma_i^{(n)}, \varsigma_j^{(n)}; \kappa_{\mathrm{p}}) \varphi_{1,D}^{(n),j} + \sum_{j=0}^{2n-1} \frac{\pi}{n} \widetilde{H}^{D,B}(\varsigma_i^{(n)}, \varsigma_j^{(n)}; \kappa_{\mathrm{s}}) \varphi_{2,D}^{(n),j} \\
& + \sum_{j=0}^{2n-1} \left(R_{|i-j|}^{(n)} \widetilde{K}_1^{B,B}(\varsigma_i^{(n)}, \varsigma_j^{(n)}; \kappa_{\mathrm{p}}) + \frac{\pi}{n} \widetilde{K}_2^{B,B}(\varsigma_i^{(n)}, \varsigma_j^{(n)}; \kappa_{\mathrm{p}}) \right) \varphi_{1,B}^{(n),j} \\
& + \sum_{j=0}^{2n-1} \left(-T_{i-j}^{(n)} \widetilde{H}_1^{B,B}(\varsigma_i^{(n)}, \varsigma_j^{(n)}; \kappa_{\mathrm{s}}) + R_{|i-j|}^{(n)} \widetilde{H}_2^{B,B}(\varsigma_i^{(n)}, \varsigma_j^{(n)}; \kappa_{\mathrm{s}}) + \frac{\pi}{n} \widetilde{H}_3^{B,B}(\varsigma_i^{(n)}, \varsigma_j^{(n)}; \kappa_{\mathrm{s}}) \right) \varphi_{2,B}^{(n),j}, \\
w_{2,B}^{(n),i} = & \varphi_{2,B}^{(n),i} + \sum_{j=0}^{2n-1} \frac{\pi}{n} \widetilde{H}^{D,B}(\varsigma_i^{(n)}, \varsigma_j^{(n)}; \kappa_{\mathrm{p}}) \varphi_{1,D}^{(n),j} - \sum_{j=0}^{2n-1} \frac{\pi}{n} \widetilde{K}^{D,B}(\varsigma_i^{(n)}, \varsigma_j^{(n)}; \kappa_{\mathrm{s}}) \varphi_{2,D}^{(n),j} \\
& + \sum_{j=0}^{2n-1} \left(-T_{i-j}^{(n)} \widetilde{H}_1^{B,B}(\varsigma_i^{(n)}, \varsigma_j^{(n)}; \kappa_{\mathrm{p}}) + R_{|i-j|}^{(n)} \widetilde{H}_2^{B,B}(\varsigma_i^{(n)}, \varsigma_j^{(n)}; \kappa_{\mathrm{p}}) + \frac{\pi}{n} \widetilde{H}_3^{B,B}(\varsigma_i^{(n)}, \varsigma_j^{(n)}; \kappa_{\mathrm{p}}) \right) \varphi_{1,B}^{(n),j} \\
& - \sum_{j=0}^{2n-1} \left(R_{|i-j|}^{(n)} \widetilde{K}_1^{B,B}(\varsigma_i^{(n)}, \varsigma_j^{(n)}; \kappa_{\mathrm{s}}) + \frac{\pi}{n} \widetilde{K}_2^{B,B}(\varsigma_i^{(n)}, \varsigma_j^{(n)}; \kappa_{\mathrm{s}}) \right) \varphi_{2,B}^{(n),j},
\end{aligned}
$$

where $w_{l,\sigma}^{(n),i} = w_{l,\sigma}(\varsigma_i^{(n)})$, $\varphi_{l,\sigma}^{(n),j} = \varphi_{l,\sigma}(\varsigma_j^{(n)})$ for $i, j = 0, \dots, 2n-1$, $l = 1, 2$, $\sigma = D, B$.

In addition, it is convenient to introduce the following definitions:

$$
\begin{aligned}
M_D(t, \varsigma; \kappa, \varphi) &:= \gamma_\kappa \exp\left\{ -\mathrm{i}\kappa \Big(c_1 \cos t + c_2 \sin t + r(\varsigma) \cos(t - \varsigma) \Big) \right\} \varphi(\varsigma), \\
M_B(t, \varsigma; \kappa, \varphi) &:= \gamma_\kappa \exp\left\{ -\mathrm{i}\kappa \Big(c_1 \cos t + c_2 \sin t + R \cos(t - \varsigma) \Big) \right\} \varphi(\varsigma), \\
S_{\kappa_{\mathrm{p}}}^{\infty}(\varsigma_i^{(\bar{n})}) &= \frac{\pi}{n} \sum_{j=0}^{2n-1} \Big(M_D(\varsigma_i^{(\bar{n})}, \varsigma_j^{(n)}; \kappa_{\mathrm{p}}, \varphi_{1,D}) + M_B(\varsigma_i^{(\bar{n})}, \varsigma_j^{(n)}; \kappa_{\mathrm{p}}, \varphi_{1,B}) \Big), \\
S_{\kappa_{\mathrm{s}}}^{\infty}(\varsigma_i^{(\bar{n})}) &= \frac{\pi}{n} \sum_{j=0}^{2n-1} \Big(M_D(\varsigma_i^{(\bar{n})}, \varsigma_j^{(n)}; \kappa_{\mathrm{s}}, \varphi_{2,D}) + M_B(\varsigma_i^{(\bar{n})}, \varsigma_j^{(n)}; \kappa_{\mathrm{s}}, \varphi_{2,B}) \Big).
\end{aligned}
$$

Then, we get the discretized linear system

$$
\begin{aligned}
& a_{\mathrm{p}} \left(\sum_{l=1}^{2} A_l^c(\varsigma_i^{(\bar{n})}; \kappa_{\mathrm{p}}, \varphi_1) \Delta c_l + \sum_{m=0}^{M} \alpha_m A_{1,m}^r(\varsigma_i^{(\bar{n})}; \kappa_{\mathrm{p}}, \varphi_1) + \sum_{m=1}^{M} \beta_m A_{2,m}^r(\varsigma_i^{(\bar{n})}; \kappa_{\mathrm{p}}, \varphi_1) \right) \\
& + a_{\mathrm{s}} \left(\sum_{l=1}^{2} A_j^c(\varsigma_i^{(\bar{n})}; \kappa_{\mathrm{s}}, \varphi_2) \Delta c_l + \sum_{m=0}^{M} \alpha_m A_{1,m}^r(\varsigma_i^{(\bar{n})}; \kappa_{\mathrm{s}}, \varphi_2) + \sum_{m=1}^{M} \beta_m A_{2,m}^r(\varsigma_i^{(\bar{n})}; \kappa_{\mathrm{s}}, \varphi_2) \right) \\
& = \breve{w}(\varsigma_i^{(\bar{n})}),
\end{aligned} \tag{5.27}
$$

which is to determine the real coefficients Δc_1, Δc_2, α_m and β_m. Here

$$
A_l^c(\varsigma_i^{(\bar{n})}; \kappa, \varphi) = 2\Re \left\{ \frac{\pi}{n} \overline{S_\kappa^{\infty}(\varsigma_i^{(\bar{n})})} \sum_{j=0}^{2n-1} L_l(\varsigma_i^{(\bar{n})}, \varsigma_j^{(n)}; \kappa, \varphi) \right\}
$$

for $l = 1, 2$, and

$$A^r_{1,m}(\varsigma_i^{(\bar{n})}; \kappa, \varphi) = 2\Re\left\{\frac{\pi}{n}\overline{S^\infty_\kappa(\varsigma_i^{(\bar{n})})}\sum_{j=0}^{2n-1} L_{3,m}(\varsigma_i^{(\bar{n})}, \varsigma_j^{(n)}; \kappa, \varphi)\right\},$$
$$A^r_{2,m}(\varsigma_i^{(\bar{n})}; \kappa, \varphi) = 2\Re\left\{\frac{\pi}{n}\overline{S^\infty_\kappa(\varsigma_i^{(\bar{n})})}\sum_{j=0}^{2n-1} L_{4,m}(\varsigma_i^{(\bar{n})}, \varsigma_j^{(n)}; \kappa, \varphi)\right\}.$$

Similarly, the overdetermined system (5.27) can be solved by using the Tikhonov regularization with an H^2 penalty term described in section 5.1.2. The details are omitted.

6. Numerical experiments. In this section, we present some numerical examples to demonstrate the feasibility of the proposed iterative reconstruction methods. In all the examples, a single shear plane wave is used to illuminate the obstacle. The synthetic compressional far-field data are numerically generated at 64 points, i.e., $\bar{n} = 32$, by using another Nyström method based on Alpert's quadrature [1] to avoid the "inverse crime" [29]. To test stability, the noisy data $u_{\infty,\delta}$ and $|u_{\infty,\delta}|^2$ are constructed in the following way:

$$u_{\infty,\delta} = u_\infty(1 + \delta\breve{\eta}), \quad |u_{\infty,\delta}|^2 = |u^\infty|^2(1 + \delta\eta),$$

where $\breve{\eta} = \breve{\eta}_1 + \mathrm{i}\breve{\eta}_2$, $\breve{\eta}_1$, $\breve{\eta}_2$, and η are normally distributed random numbers ranging in $[-1, 1]$, $\delta > 0$ is the relative noise level. In addition, we denote the L^2 relative error between the reconstructed and exact boundaries by

$$\mathrm{Err}_k := \frac{\|p_D^{(k)} - p_D\|_{L^2(\Omega)}}{\|p_D\|_{L^2(\Omega)}}.$$

In the iteration, we obtain the update ξ from a scaled Newton step by using the Tikhonov regularization and H^2 penalty term, i.e.,

$$\xi = \rho\Big(\lambda\widetilde{I} + \Re(\widetilde{B}^*\widetilde{B})\Big)^{-1}\Re(\widetilde{B}^*\widetilde{w}),$$

where the scaling factor $\rho \geq 0$ is fixed throughout the iterations. Analogously to [10], the regularization parameters λ in (5.13) are chosen as

$$\lambda_k := \left\|a_{\mathrm{p}}\Big(\phi_\infty - S^\infty_{\kappa_{\mathrm{p}}}(p^{(k-1)}, \varphi_1^{(k-1)})\Big) + a_{\mathrm{s}}\Big(\psi_\infty - S^\infty_{\kappa_{\mathrm{s}}}(p^{(k-1)}, \varphi_2^{(k-1)})\Big)\right\|_{L^2}, \ k = 1, 2, \ldots.$$

In all of the following figures, the exact boundary curves are displayed by solid lines, the reconstructed boundary curves are depicted by dashed lines $--$, and all the initial guesses are taken to be a circle with radius $r^{(0)} = 0.3$ which is indicated by the dash-dotted lines $\cdot-$. The incident directions are denoted by directed line segments with arrows. Throughout all the numerical examples, we take $\lambda = 3.88, \mu = 2.56$, the scaling factor $\rho = 0.9$, and the truncation $M = 6$. The number of quadrature points is equal to 128, i.e., $n = 64$. In addition, we choose

Table 1
Parametrization of the exact boundary curves.

Type	Parametrization
Apple-shaped obstacle	$p_D(t) = \frac{0.55(1+0.9\cos t+0.1\sin 2t)}{1+0.75\cos t}(\cos t, \sin t), \quad t \in [0, 2\pi]$
Peanut-shaped obstacle	$p_D(t) = 0.5\sqrt{0.25\cos^2 t + \sin^2 t}(\cos t, \sin t), \quad t \in [0, 2\pi]$

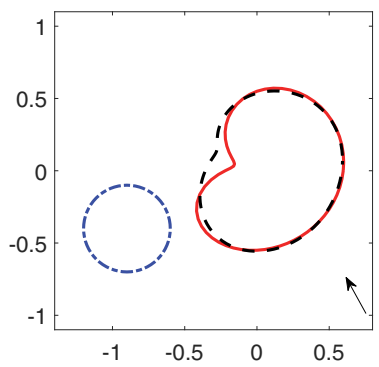

(a) Reconstruction with 1% noise, $\epsilon = 0.01$

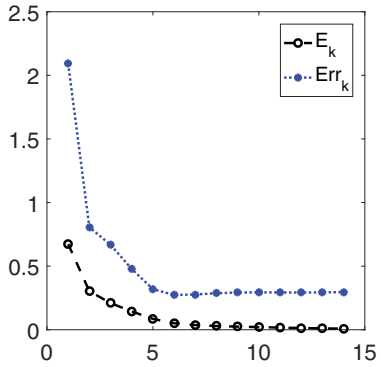

(b) Relative error with 1% noise

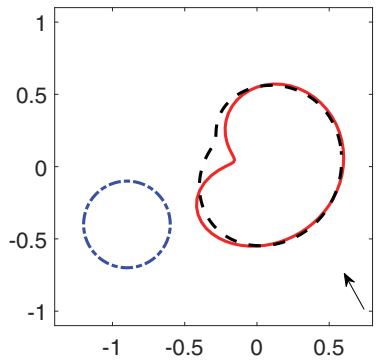

(c) Reconstruction with 5% noise, $\epsilon = 0.025$

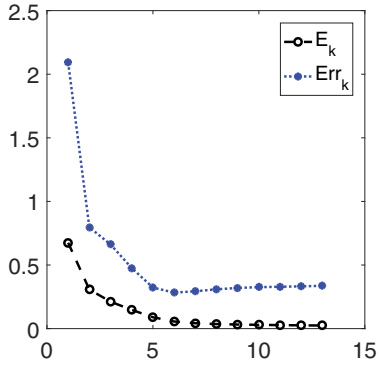

(d) Relative error with 5% noise

Figure 2. *Reconstructions of an apple-shaped obstacle with phased data at different levels of noise (see Example 1). The initial guess is given by* $(c_1^{(0)}, c_2^{(0)}) = (-0.9, 0.4), r^{(0)} = 0.3$, *and the incident angle* $\theta = 5\pi/8$.

the angular frequency $\omega = 0.7\pi$ in Example 1 and $\omega = 0.6\pi$ in Examples 2 and 3. We present the results for two commonly used examples: an apple-shaped obstacle and a peanut-shaped obstacle. The parametrization of the exact boundary curves for these two obstacles are given in Table 1.

6.1. Example 1: The phased IOSP. We consider an inverse elastic scattering problem of reconstructing a rigid obstacle from the phased far-field data by using Algorithm 1. In Figures 2 and 3, the results are shown for the apple-shaped obstacle and the peanut-shaped

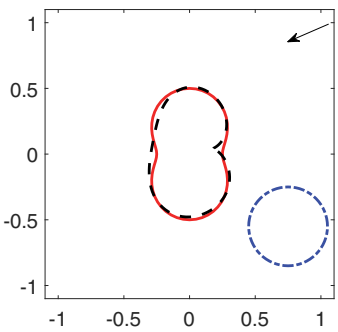

(a) Reconstruction with 1% noise, $\epsilon = 0.006$

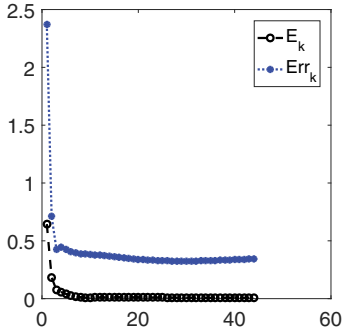

(b) Relative error with 1% noise

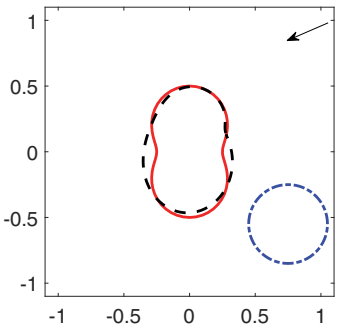

(c) Reconstruction with 5% noise, $\epsilon = 0.025$

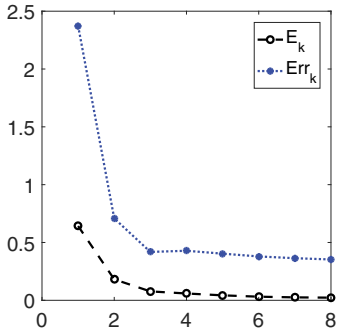

(d) Relative error with 5% noise

Figure 3. *Reconstructions of a peanut-shaped obstacle with phased data at different levels of noise (see Example* 1*). The initial guess is given by* $(c_1^{(0)}, c_2^{(0)}) = (0.75, -0.55), r^{(0)} = 0.3$*, and the incident angle* $\theta = 7\pi/6$*.*

obstacles with 1% and 5% noise, respectively. The relative L^2 error Err_k between the reconstructed obstacle and the exact obstacle and the relative error estimator E_k defined in (5.9) are plotted against the number of iterations. As can be seen from the error curves, the relative error estimator E_k follows the actual relative error Err_k very well and is a reasonable choice of the stopping criteria for the iterations. For the fixed incident direction, Figures 4 and 5 show the reconstructions of the apple-shaped obstacle and the peanut-shaped obstacle by using different initial guesses; for the fixed initial guess, Figures 6 and 7 show the reconstructions of the apple-shaped obstacle and the peanut-shaped obstacle by using different incident directions. As shown in these results, the reconstruction is not sensitive to the initial guess or the incident direction. The location and shape of the obstacle can be simultaneously and satisfactorily reconstructed for a single incident plane wave.

6.2. Example 2: The phased IOSP with a reference ball. Now we investigate the inverse scattering problem of reconstructing a rigid obstacle from the phased far-field data by introducing a reference ball. The reconstructions with 1% noise and 5% noise for the apple-shaped and peanut-shaped obstacles are shown in Figures 8 and 9, respectively. The relative L^2 error Err_k and the relative error estimator E_k are also presented in the figures. Tests are also done by using different initial guesses and different incident directions. In addition, we test

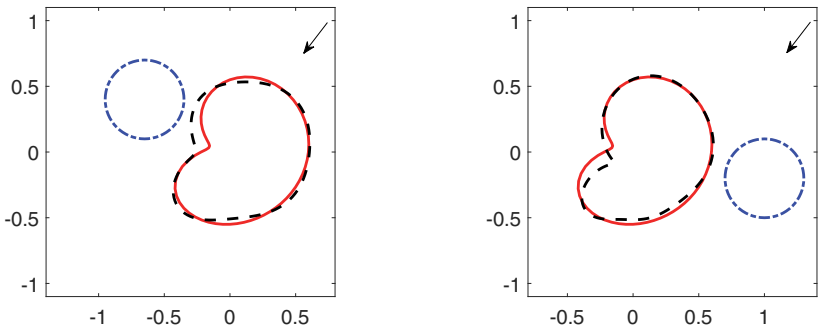

Figure 4. *Reconstructions of an apple-shaped obstacle with different initial guesses, where 1% noise is added and the incident angle $\theta = 4\pi/3$ (see Example 1). (left) $(c_1^{(0)}, c_2^{(0)}) = (-0.65, 0.4)$, $r^{(0)} = 0.3$, $\epsilon = 0.015$; (right) $(c_1^{(0)}, c_2^{(0)}) = (1, -0.2)$, $r^{(0)} = 0.3$, $\epsilon = 0.01$.*

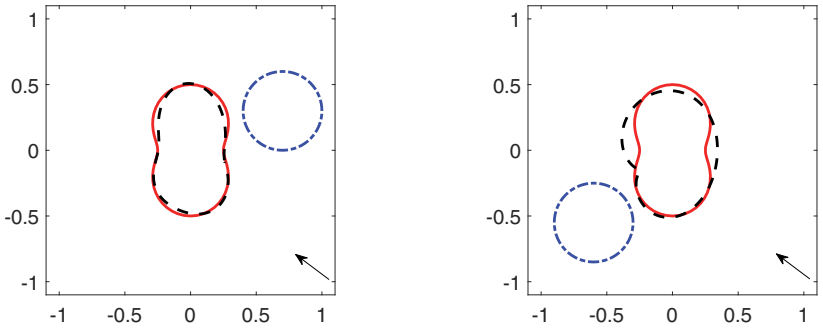

Figure 5. *Reconstructions of a peanut-shaped obstacle with different initial guesses, where 1% noise is added and the incident angle $\theta = 7\pi/4$ (see Example 1). (left) $(c_1^{(0)}, c_2^{(0)}) = (0.7, 0.3)$, $r^{(0)} = 0.3$, $\epsilon = 0.01$; (right) $(c_1^{(0)}, c_2^{(0)}) = (-0.6, -0.55)$, $r^{(0)} = 0.3$, $\epsilon = 0.025$.*

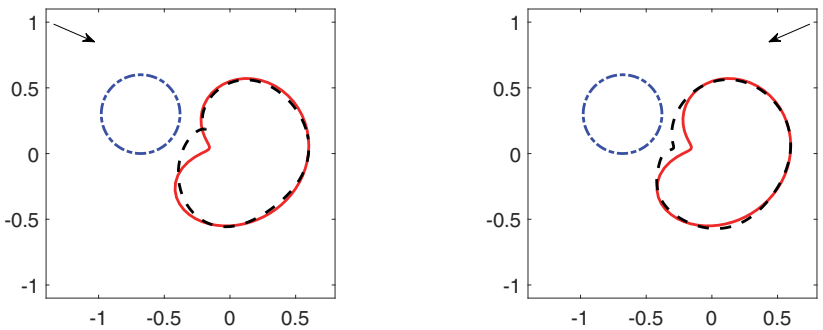

Figure 6. *Reconstructions of an apple-shaped obstacle with different incident directions, where 1% noise is added and the initial guess is given by $(c_1^{(0)}, c_2^{(0)}) = (-0.7, 0.3)$, $r^{(0)} = 0.3$ (see Example 1). (left) incident angle $\theta = 11\pi/6$, $\epsilon = 0.01$; (right) incident angle $\theta = 7\pi/6$, $\epsilon = 0.01$.*

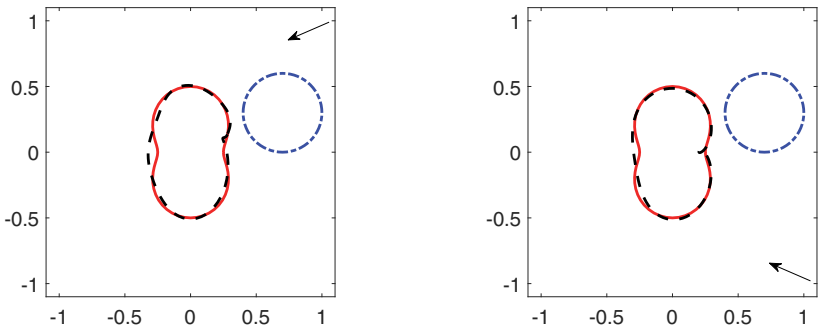

Figure 7. *Reconstructions of a peanut-shaped obstacle with different incident directions, where* 1% *noise is added and the initial guess is given by* $(c_1^{(0)}, c_2^{(0)}) = (0.7, 0.3)$, $r^{(0)} = 0.3$ *(see Example* 1*). (left) incident angle* $\theta = 7\pi/6$, $\epsilon = 0.006$*; (right) incident angle* $\theta = 5\pi/6$, $\epsilon = 0.006$.

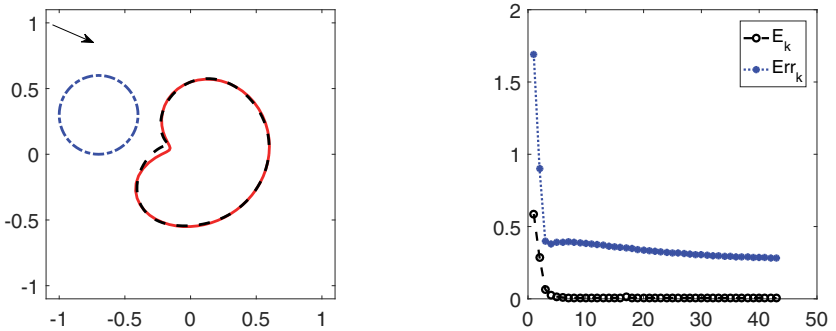

(a) Reconstruction with 1% noise, $\epsilon = 0.005$ (b) Relative error with 1% noise

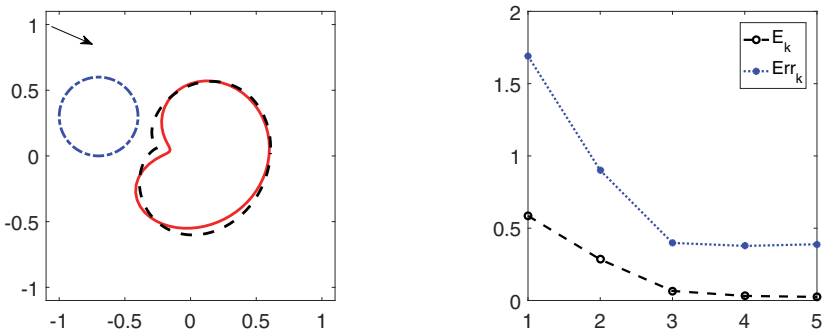

(c) Reconstruction with 5% noise, $\epsilon = 0.025$ (d) Relative error with 5% noise

Figure 8. *Reconstructions of an apple-shaped obstacle with phased data at different levels of noise and a reference ball (see Example* 2*). The initial guess is given by* $(c_1^{(0)}, c_2^{(0)}) = (-0.7, 0.3), r^{(0)} = 0.3$*, the incident angle* $\theta = 11\pi/6$*, and the reference ball is* $(b_1, b_2) = (5, 0), R = 0.5$.

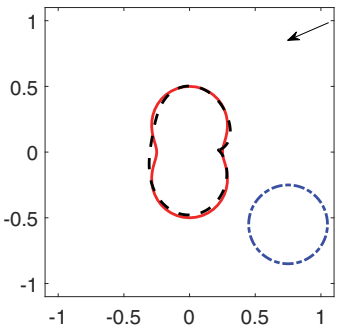

(a) Reconstruction with 1% noise, $\epsilon = 0.006$

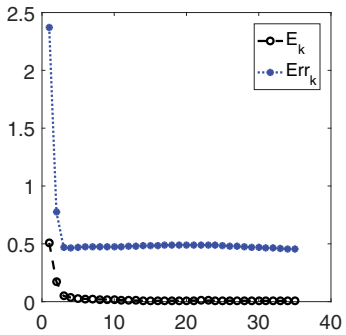

(b) Relative error with 1% noise

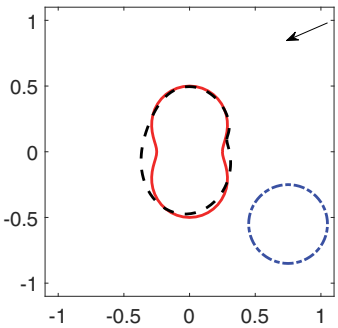

(c) Reconstruction with 5% noise, $\epsilon = 0.025$

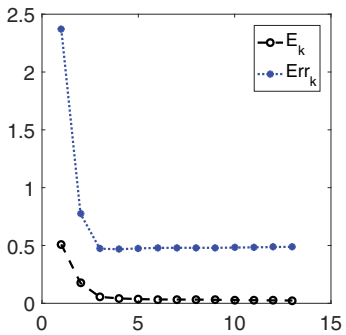

(d) Relative error with 5% noise

Figure 9. *Reconstructions of a peanut-shaped obstacle with phased data at different levels of noise and a reference ball (see Example 2). The initial guess is given by* $(c_1^{(0)}, c_2^{(0)}) = (0.75, -0.55), r^{(0)} = 0.3$*, the incident angle* $\theta = 7\pi/6$*, and the reference ball is* $(b_1, b_2) = (9, 0), R = 0.5$.

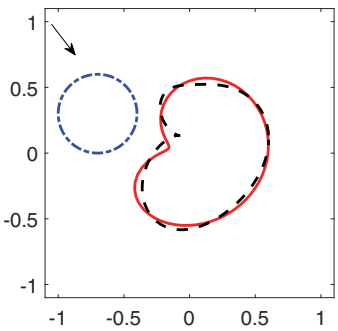

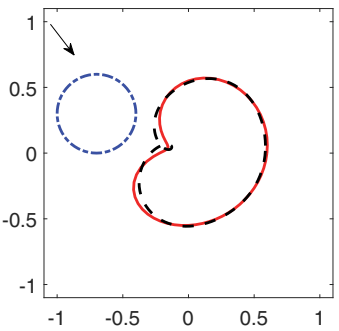

Figure 10. *Reconstructions of an apple-shaped obstacle with different reference balls, where* 1% *noise is added, the incident angle* $\theta = 5\pi/3$*, and the initial guess is given by* $(c_1^{(0)}, c_2^{(0)}) = (-0.7, 0.3), r^{(0)} = 0.3$ *(see Example 2). (left)* $(b_1, b_2) = (5, 0), R = 0.4$*,* $\epsilon = 0.01$*; (right)* $(b_1, b_2) = (6, 0), R = 0.9$*,* $\epsilon = 0.006$.

the influence by using reference balls with different radii and locations. For the fixed initial guess and incident direction, Figures 10 and 11 show the reconstructions of the apple-shaped obstacle and the peanut-shaped obstacle by using different reference balls. The reconstructed

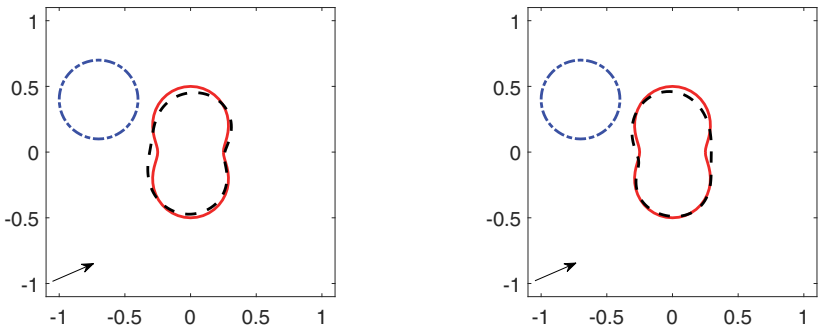

Figure 11. *Reconstructions of a peanut-shaped obstacle with different reference balls, where* 1% *noise is added, the incident angle* $\theta = \pi/6$*, and the initial guess is given by* $(c_1^{(0)}, c_2^{(0)}) = (-0.7, 0.4)$*,* $r^{(0)} = 0.3$ *(see Example* 2*). (left)* $(b_1, b_2) = (7.5, 0), R = 0.6$*,* $\epsilon = 0.01$*; (right)* $(b_1, b_2) = (0, 7), R = 0.6$*,* $\epsilon = 0.01$*.*

obstacles agree very well with exact ones. As can be seen, the results by using the reference ball technique are comparable with those without the reference ball in Example 1. The method works very well to reconstruct the location and the shape.

6.3. Example 3: The phaseless IOSP with a reference ball. By adding a reference ball to the inverse scattering system, we consider the inverse scattering problem of reconstructing a rigid obstacle from phaseless far-field data by using Algorithm 2. The reconstructions with 1% noise and 5% noise are shown in Figures 12 and 13. Again, the relative L^2 error Err_k and the relative error estimator E_k are plotted in the figures. Figures 14 and 15 show the reconstructions of the apple-shaped obstacle and the peanut-shaped obstacle by using different reference balls. From these figures, we observe that the translation invariance property of the phaseless far-field pattern can be broken by introducing a reference ball. Based on this technique, both the location and shape of the obstacle can be satisfactorily reconstructed from the phaseless far-field data by using a single incident plane wave.

7. Conclusions and future works. In this paper, we have studied the two-dimensional inverse elastic scattering problem by the phased and phaseless far-field data for a single incident plane wave. Based on the Helmholtz decomposition, the elastic wave equation is reformulated into a coupled boundary value problem of the Hemholtz equation. The relationship between compressional or shear far-field pattern for the Navier equation and the corresponding far-field pattern for the Helmholtz equation are investigated. The translation invariance property of the phaseless compressional and shear far-field pattern is proved. A nonlinear integral equation method is developed for the inverse problem. For the phaseless data, we introduce a reference ball technique to the inverse scattering system in order to break the translation invariance. Numerical examples are presented to demonstrate the effectiveness and stability of the proposed method. Future work includes the different boundary conditions of the obstacle and the three-dimensional problem. It is a challenging problem for the uniqueness of the phaseless inverse elastic scattering problem with a reference ball. We intend to investigate these issues and report the progress elsewhere.

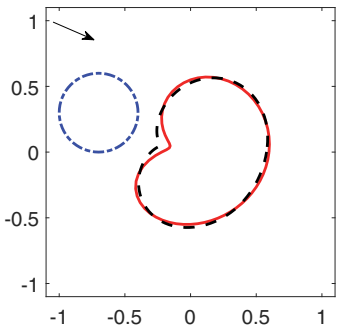

(a) Reconstruction with 1% noise, $\epsilon = 0.005$

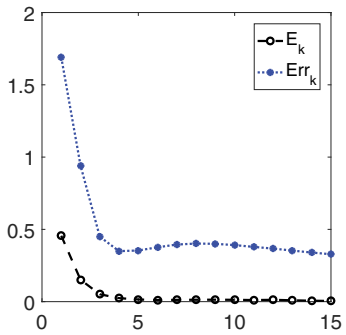

(b) Relative error with 1% noise

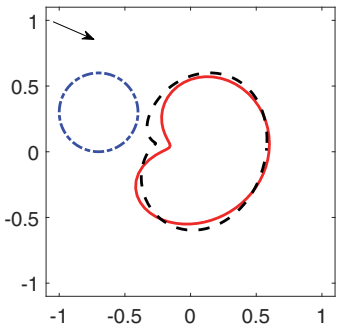

(c) Reconstruction with 5% noise, $\epsilon = 0.025$

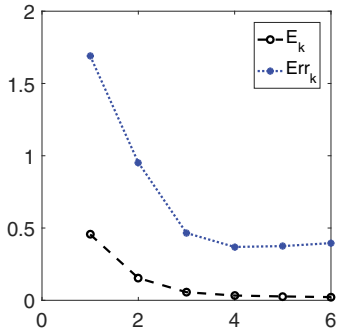

(d) Relative error with 5% noise

Figure 12. *Reconstructions of an apple-shaped obstacle with different levels of noise by using phaseless data and a reference ball (see Example 3). The initial guess is given by* $(c_1^{(0)}, c_2^{(0)}) = (-0.7, 0.3), r^{(0)} = 0.3$*, the incident angle* $\theta = 11\pi/6$*, and the reference ball is* $(b_1, b_2) = (5, 0), R = 0.5$.

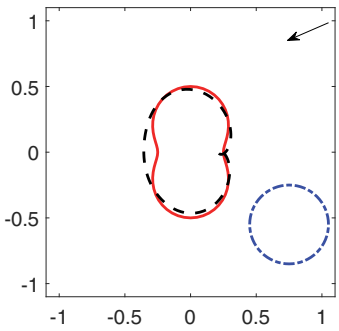

(a) Reconstruction with 1% noise, $\epsilon = 0.02$

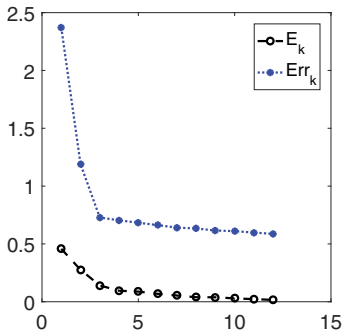

(b) Relative error with 1% noise

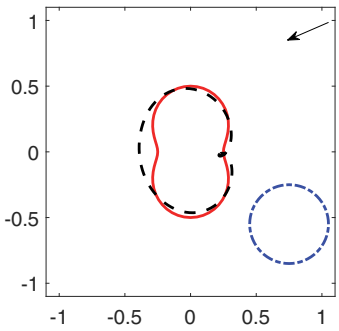

(c) Reconstruction with 5% noise, $\epsilon = 0.04$

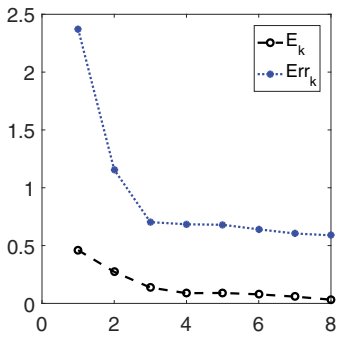

(d) Relative error with 5% noise

Figure 13. *Reconstructions of a peanut-shaped obstacle with different levels of noise by using phaseless data and a reference ball (see Example 3). The initial guess is given by* $(c_1^{(0)}, c_2^{(0)}) = (0.75, -0.55), r^{(0)} = 0.3$, *the incident angle* $\theta = 7\pi/6$, *and the reference ball is* $(b_1, b_2) = (9, 0), R = 0.5$.

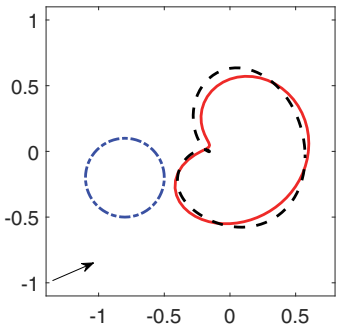

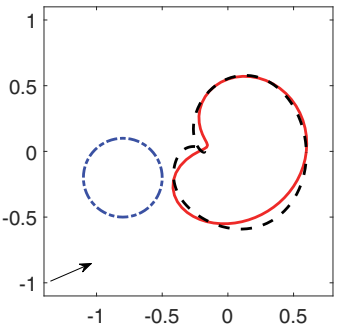

Figure 14. *Reconstructions of an apple-shaped obstacle with different reference balls, where 1% noise is added, the incident angle* $\theta = \pi/6$, *and the initial guess is given by* $(c_1^{(0)}, c_2^{(0)}) = (-0.8, -0.2), r^{(0)} = 0.3$ *(see Example 3). (left)* $(b_1, b_2) = (5.5, 0), R = 0.5, \epsilon = 0.01$*; (right)* $(b_1, b_2) = (-8.5, 0), R = 0.4, \epsilon = 0.015$.

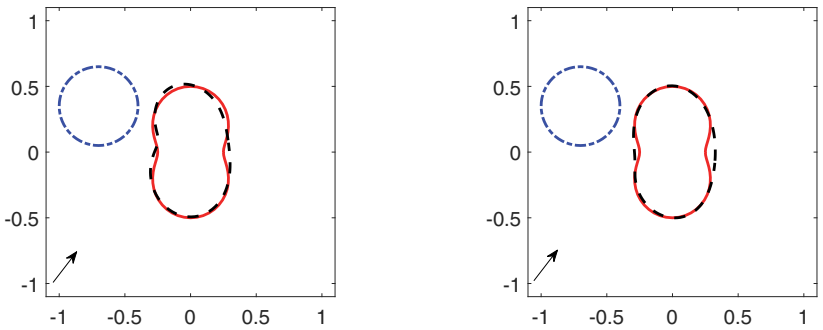

Figure 15. *Reconstructions of a peanut-shaped obstacle with different reference balls, where* 1% *noise is added, the incident angle* $\theta = \pi/3$*, and the initial guess is given by* $(c_1^{(0)}, c_2^{(0)}) = (-0.7, 0.35), r^{(0)} = 0.3$ *(see Example* 3*). (left)* $(b_1, b_2) = (6, 0), R = 0.6$*,* $\epsilon = 0.006$*; (right)* $(b_1, b_2) = (7.5, 0), R = 1.5$*,* $\epsilon = 0.006$*.*

REFERENCES

[1] B. K. Alpert, *Hybrid Gauss-trapezoidal quadrature rules*, SIAM J Sci. Comput., 20 (1999), pp. 1551–1584.

[2] H. Ammari, E. Bretin, J. Garnier, H. Kang, H. Lee, and A. Wahab, *Mathematical Methods in Elasticity Imaging*, Princeton University Press, Princeton, NJ, 2015.

[3] H. Ammari, Y. T. Tin, and J. Zou, *Phased and phaseless domain reconstructions in the inverse scattering problem via scattering coefficients*, SIAM J. Appl. Math., 76 (2016), pp. 1000–1030.

[4] T. Arens, *Linear sampling method for* 2*D inverse elastic wave scattering*, Inverse Problems, 17 (2001), pp. 1445–1464.

[5] G. Bao and L. Zhang, *Shape reconstruction of the multi-scale rough surface from multi-frequency phaseless data*, Inverse Problems, 32 (2016), 085002.

[6] G. Bao, P. Li, and J. Lv, *Numerical solution of an inverse diffraction grating problem from phaseless data*, J. Opt. Soc. Amer. A, 30 (2013), pp. 293–299.

[7] M. Bonnet and A. Constantinescu, *Inverse problems in elasticity*, Inverse Problems, 21 (2005), pp. 1–50.

[8] Z. Chen and G. Huang, *A direct imaging method for electromagnetic scattering data without phase information*, SIAM J. Imaging Sci., 9 (2016), pp. 1273–1297.

[9] D. Colton and R. Kress, *Inverse Acoustic and Electromagnetic Scattering Theory*, 3rd ed., Springer, New York, 2013.

[10] H. Dong, D. Zhang, and Y. Guo, *A reference ball based iterative algorithm for imaging acoustic obstacle from phaseless far-field data*, Inverse Probl. Imaging, 13 (2019), pp. 177–195.

[11] J. Elschner and M. Yamamoto, *Uniqueness in inverse elastic scattering with finitely many incident waves*, Inverse Problems, 26 (2010), 045005.

[12] P. Gao, H. Dong, and F. Ma, *Inverse scattering via nonlinear integral equations method for a sound-soft crack from phaseless data*, Appl. Math., 63 (2018), pp. 149–165.

[13] P. Hähner, *A uniqueness theorem in inverse scattering of elastic waves*, J. Appl. Math., 51 (1993), pp. 201–215.

[14] P. Hähner and G. C. Hsiao, *Uniqueness theorems in inverse obstacle scattering of elastic waves*, Inverse Problems, 9 (1993), pp. 525–534.

[15] G. Hu. A. Kirsch, and M. Sini, *Some inverse problems arising from elastic scattering by rigid obstacles*, Inverse Problems, 29 (2013), 015009

[16] G. Hu, J. Li, H. Liu, and H. Sun, *Inverse elastic scattering for multiscale rigid bodies with a single far-field pattern*, SIAM J. Imaging Sci., 7 (2014), pp. 1799–1825.

[17] O. Ivanyshyn, *Shape reconstruction of acoustic obstacles from the modulus of the far field pattern*, Inverse Probl. Imaging, 1 (2007), pp. 609–622.

[18] O. Ivanyshyn and R. Kress, *Identification of sound-soft 3D obstacles from phaseless data*, Inverse Probl. Imaging, 4 (2010), pp. 131–149.
[19] T. Johansson and B. D. Sleeman, *Reconstruction of an acoustically sound-soft obstacle from one incident field and the far-field pattern*, IMA J. Appl. Math., 72 (2007), pp. 96–112.
[20] M. Kar and M. Sini, *On the inverse elastic scattering by interfaces using one type of scattered waves*, J. Elasticity, 118 (2015), pp. 15–38.
[21] A. Karageorghis, B.T. Johansson, and D. Lesnic, *The method of fundamental solutions for the identification of a sound-soft obstacle in inverse acoustic scattering*, Appl. Numer. Math., 62 (2012), pp. 1767–1780.
[22] M. V. Klibanov, *Phaseless inverse scattering problems in three dimensions*, SIAM J. Appl. Math., 74 (2014), pp. 392–410.
[23] M. V. Klibanov, D. Nguyen, and L. Nguyen, *A coefficient inverse problem with a single measurement of phaseless scattering data*, SIAM J. Appl. Math., 79 (2019), pp. 1–27.
[24] R. Kress, *On the numerical solution of a hypersingular integral equation in scattering theory*, J. Comput. Appl. Math., 61 (1995), pp. 345–360.
[25] R. Kress, *Inverse elastic scattering from a crack*, Inverse Problems, 12 (1996), pp. 667–684.
[26] R. Kress, *Newton's method for inverse obstacle scattering meets the method of least squares*, Inverse Problems, 19 (2003), pp. S91–S104.
[27] R. Kress, *Linear Integral Equations*, 3rd ed., Springer, New York, 2014.
[28] R. Kress and W. Rundell, *Inverse obstacle scattering with modulus of the far field pattern as data*, in Inverse Problems in Medical Imaging and Nondestructive Testing, Springer, Vienna, 1997, pp. 75–92.
[29] J. Lai and P. Li, *A Fast Solver for the Elastic Scattering of Multiple Particles*, preprint, arXiv:1812.05232, 2018.
[30] L. D. Landau and E. M. Lifshitz, *Theory of Elasticity*, Pergamon, Oxford, 1986.
[31] F. Le Louër, *A domain derivative-based method for solving elastodynamic inverse obstacle scattering problems*, Inverse Problems, 31 (2015), 115006.
[32] F. Le Louër, *On the Fréchet derivative in elastic obstacle scattering*, SIAM J. Appl. Math., 72 (2012), pp. 1493–1507.
[33] K. M. Lee, *Shape reconstructions from phaseless data*, Eng. Anal. Bound. Elem., 71 (2016), pp. 174–178.
[34] J. Li, H. Liu, and Y. Wang, *Recovering an electromagnetic obstacle by a few phaseless backscattering measurements*, Inverse Problems, 33 (2017), 035011.
[35] J. Li, H. Liu, and J. Zou, *Strengthened linear sampling method with a reference ball*, SIAM J. Sci. Comput., 31 (2010), pp. 4013–4040.
[36] P. Li, Y. Wang, Z. Wang, and Y. Zhao, *Inverse obstacle scattering for elastic waves*, Inverse Problems, 32 (2016), 115018.
[37] P. Li, Y. Wang, and Y. Zhao, *Inverse elastic surface scattering with near-field data*, Inverse Problems, 31 (2015), 035009.
[38] X. Liu and B. Zhang, *Unique determination of a sound-soft ball by the modulus of a single far field datum*, J. Math. Anal. Appl., 365 (2010), pp. 619–624.
[39] X. Ji, X. Liu, and B. Zhang, *Target reconstruction with a reference point scatterer using phaseless far field patterns*, SIAM J. Imaging Sci., 12 (2019), pp. 372–391.
[40] G. Nakamura and G. Uhlmann, *Inverse problems at the boundary of elastic medium*, SIAM J. Math. Anal., 26 (1995), pp. 263–279.
[41] X. Xu, B. Zhang, and H. Zhang, *Uniqueness in inverse scattering problems with phaseless far-field data at a fixed frequency*, SIAM J. Appl. Math., 78 (2018), pp. 1737–1753.
[42] J. Yue, M. Li, P. Li, and X. Yuan, *Numerical solution of an inverse obstacle scattering problem for elastic waves via the Helmholtz decomposition*, Commun. Comput. Phys., to appear.
[43] D. Zhang and Y. Guo, *Uniqueness results on phaseless inverse scattering with a reference ball*, Inverse Problems, 34 (2018), 085002.
[44] D. Zhang, Y. Guo, J. Li, and H. Liu, *Retrieval of acoustic sources from multi-frequency phaseless data*, Inverse Problems, 34 (2018), 094001.
[45] B. Zhang and H. Zhang, *Recovering scattering obstacles by multi-frequency phaseless far-field data*, J. Comput. Phys., 345 (2017), pp. 58–73.
[46] B. Zhang and H. Zhang, *Fast imaging of scattering obstacles from phaseless far-field measurements at a fixed frequency*, Inverse Problems, 34 (2018), 104005.